J. Fluid Mech. (2020), *vol.* 894, A6.
Published by Cambridge University Press
doi:10.1017/jfm.2020.247

Frequency selection in a gravitationally stretched capillary jet in the jetting regime

Isha Shukla[1] **and François Gallaire**[1],†

[1]Laboratory of Fluid Mechanics and Instabilities, École Polytechnique Fédérale de Lausanne, 1015 Lausanne, Switzerland

(Received 31 July 2019; revised 4 February 2020; accepted 23 March 2020)

A capillary jet falling under the effect of gravity continuously stretches while thinning downstream. We report here the effect of external periodic forcing on such a spatially varying jet in the jetting regime. Surprisingly, the optimal forcing frequency producing the most unstable jet is found to be highly dependent on the forcing amplitude. Taking benefit of the one-dimensional Eggers & Dupont (*J. Fluid Mech.*, vol. 262, 1994, pp. 205–221) equations, we investigate the case through nonlinear simulations and linear stability analysis. In the local framework, the WKBJ (Wentzel–Kramers–Brillouin–Jeffreys) formalism, established for weakly non-parallel flows, fails to capture the nonlinear simulation results quantitatively. However, in the global framework, the resolvent analysis, supplemented by a simple approximation of the required response norm inducing breakup, is shown to correctly predict the optimal forcing frequency at a given forcing amplitude and the resulting jet breakup length. The results of the resolvent analysis are found to be in good agreement with those of the nonlinear simulations.

Key words: capillary flows, absolute/convective instability

1. Introduction

Pele's hair, which are thin strands of volcanic glass formed in the air during the fountaining of molten lava, is an impressive example of the stretching ability of highly viscous fluids. Named after Pele, the Hawaiian goddess of volcanoes, a single strand with a diameter of less than 0.5 mm can extend up to a length of 2 m (Shimozuru 1994; Eggers & Villermaux 2008). If such viscous strands are pinned at one end, as in the case of honey dripping from a spoon under its own weight, gravity acts as the stretching tool for the viscous fluid, producing very thin and stable liquid threads (Senchenko & Bohr 2005; Javadi *et al.* 2013). The cross-section of such threads varies continually as the jet accelerates downstream in the direction of gravity, before breaking into drops.

Physically, the breakup of the jet into drops begins with the excitation of a suitable temporally or spatially amplifying mode due to weak external disturbances. In practice, this weak agitation is usually imposed by a controlled harmonic perturbation, either

† Email address for correspondence: francois.gallaire@epfl.ch

from within or at the outlet of the nozzle, to generate spatially amplifying waves leading to jet breakup. In this direction, the primary objective of this paper is to evaluate the response of an incompressible jet, falling in the presence of gravity, to externally imposed harmonic perturbations characterised by a fixed frequency and amplitude, and to find the optimal forcing that generates the most amplified response.

The external forcing is vital in the production of controlled micrometre-sized droplets, a feature essential to several application as in inkjet printers (Basaran 2002; Wijshoff 2010; Basaran, Gao & Bhat 2013), pharmaceuticals (Bennett *et al.* 2002) and powder technology (van Deventer, Houben & Koldeweij 2013), to name but a few. In view of the limitations linked to the fabrication of such small droplets, most of the devices used for the production of drops depend on the generation of very thin liquid threads whose diameters are several orders of magnitude smaller than the nozzle diameter. Some common methods for producing such threads use tangential electrical stresses (in electrospinning devices (Doshi & Reneker 1995; Loscertales *et al.* 2002)), outer co-flows (Marín, Campo-Cortés & Gordillo 2009) or a rotating spinneret (in fibre spinning applications (Pearson & Matovich 1969)). Rubio-Rubio, Sevilla & Gordillo (2013) showed an alternative method for producing highly elongated jets through the use of gravity, in which the mass conservation of the liquid jet forces its thinning as the liquid accelerates downstream.

The breakup of a liquid thread into drops, governed by the relative strength of the surface tension effect over the viscous and inertial effects, was first explained by Plateau (1873) and Rayleigh (1879) for a uniform column of fluid. What adds complexity to the well-understood viscous jet breakup mechanism is the presence of gravity, which significantly stretches the base flow shape. The stability of the such spatially varying gravity jets should ideally be examined using global stability analysis and by including the non-parallel effects of the base flow. A similar difficulty linked to the non-parallel nature of the flow results from the adaptation of the flow from a wall-bounded flow within the nozzle to a free jet (Sevilla 2011). Turning back to falling jets stretched by gravity, Le Dizès (1997) and later on Sauter & Buggisch (2005) were among the first to approach the problem theoretically by defining a linear global mode that correlated with the self-sustained oscillations of the falling jet, observed during the jetting (globally stable) to dripping (globally unstable) transition. The work of Sauter & Buggisch (2005) was extended by Rubio-Rubio *et al.* (2013) experimentally and theoretically by increasing the range of liquid viscosities and nozzle diameters. Additionally they retained the entire expression of the curvature term for the formulation of their stability analysis, a feature that helped them to accurately predict the critical flow rate for the stability transition and the oscillating mode compared to the previous authors. However, none of these studies predicted the jet stable length as a function of the flow rate and fluid properties, a question that was pursued by Javadi *et al.* (2013) experimentally and theoretically.

More recently, Le Dizès & Villermaux (2017) determined theoretically the stable jet length, wavelength at breakup and resulting drop size due to the most dangerous perturbation either applied at the nozzle exit or affecting the jet all along its length for different jet viscosities. Their analysis accounted for both the base-state deformation and modification of local instability dispersion relation as the jet thins in the direction of gravity. Notably, extending the work of previous authors (Tomotika 1936; Frankel & Weihs 1985; Leib & Goldstein 1986; Frankel & Weihs 1987; Sauter & Buggisch 2005; Senchenko & Bohr 2005; Javadi *et al.* 2013) they used the local plane-wave decomposition – the WKBJ (Wentzel–Kramers–Brillouin–Jeffreys) approximation –

for their analysis. It is important to note that the perturbation gain definitions used by Le Dizès & Villermaux (2017) and Javadi *et al.* (2013) were different. Le Dizès & Villermaux (2017) defined the gain as the exponential of the spatial growth rate, whereas Javadi *et al.* (2013) expressed the gain using the exponential of the temporal growth rate. Additionally, Le Dizès & Villermaux (2017) computed the resulting gain from a perturbation by considering only the exponential (e) terms of the WKBJ approximation. Finally, an *ad hoc* spatial gain of e^7 of the linear perturbations was assumed to be sufficient for breakup. Thus the level of noise was considered fixed for all the theoretical analysis.

For non-parallel flows other than the free interface jet under gravity, the successful implementation of the WKBJ approximation has been performed by Gaster, Kit & Wygnanski (1985), Huerre & Rossi (1998) and Viola, Arratia & Gallaire (2016), among others, for analysing the dominant frequency selection mechanism in shear layers and trailing vortices. In the latter reference, an excellent agreement was observed between the WKBJ approach and a so-called resolvent analysis, which consists in determining the optimal time-periodic forcing that maximises the permanent response norm. In other words, it consists in maximising the transfer function norm (Trefethen *et al.* 1993) for each frequency. This method was first applied to parallel flows characterised by a non-normal linearised stability operator, like plane Couette or plane Poiseuille flow (see Schmid & Henningson 1994), and later to non-parallel flows (Åkervik *et al.* 2008; Alizard, Cherubini & Robinet 2009; Nichols & Lele 2010). The principal aspect of the resolvent analysis lies in its ability to capture the entire non-normal flow behaviour by evaluating the resolvent norm directly from the linearised Navier–Stokes operator (Marquet & Sipp 2010; Monokrousos *et al.* 2010; Nichols & Lele 2011; Sipp & Marquet 2013; Boujo & Gallaire 2015). Following a similar approach, Garnaud *et al.* (2013) provided the preferred frequency selection and the associated spatial structures for non-parallel jet flows.

In this paper, we go beyond the global stability analysis of the gravity jets, and always operate in the stable regime where the jet behaves inherently as an amplifier. Precisely, we look at the receptivity of the jet in this regime to external perturbations, through nonlinear simulations and resolvent analysis, with the aim of finding the optimal forcing that results in the most amplified disturbance. We consider an external forcing characterised by different amplitudes. The effect of forcing amplitude on the breakup length of very high-speed jets has been numerically analysed by Hilbing & Heister (1996). However, a clear understanding of its effect in the case of spatially varying jets is still missing. Our analysis exemplifies the effect of forcing amplitude on the breakup length and the optimal forcing frequency. We also investigate the jet response using the WKBJ approximation and assess its validity for the spatially varying gravity jet. Our entire study is based on the slender-jet approximation (Eggers & Dupont 1994) of the Navier–Stokes equation for an axisymmetric jet. The reduced one-dimensional (1-D) model has turned out to be extremely valuable for the realistic representation of jets (Ambravaneswaran, Wilkes & Basaran 2002; van Hoeve *et al.* 2010) by accurately capturing the jet interface close to the breakup as well as the formation of 'satellite' drops. These equations are similar to the 1-D models for slender axisymmetric viscous liquid jets of García & Castellanos (1994), who deduced not only the same leading-order 1-D equations, but also higher-order equations like the parabolic and averaged 1-D models. During the final stage of this work, we became aware of the work of Consoli-Lizzi, Coenen & Sevilla (2014), which is further detailed in Consoli-Lizzi (2016). With an identical aim to ours, the

authors compared a linear response analysis to experimental results of forced and unforced jets. In particular, their global response frequency analysis revealed the dependence of the optimal frequency on the forcing amplitude (for forced jets) or on the noise level (in the case of unforced jets).

The paper is structured as follows. In § 2 we describe the governing equations. Then in § 3 we discuss the nonlinear simulations where the results are detailed in § 3.3. The local stability analysis of the gravity jet is performed in § 4, where we compare the jet response using stability analysis in § 4.3 and the WKBJ formulation in § 4.4. We then operate in the global framework in § 5, where the significance of the resolvent analysis is elucidated in § 5.2. We show that the resolvent analysis is self-sufficient in predicting the optimal forcing frequency and the breakup length as obtained through the nonlinear simulations. Finally, we apply a white-noise disturbance on the jet inlet to explore its behaviour in comparison to the expected response to the optimal forcing in § 6. The conclusion and some perspectives related to the present work are summarised in § 7.

2. Mathematical formulation

We consider an axisymmetric viscous jet falling vertically from a nozzle under the effect of gravity g. At the nozzle outlet, the jet has a fixed radius $\bar{h}_0$ and velocity $\bar{u}_0$. The surrounding medium is considered evanescent and is neglected. The density, dynamic viscosity and surface tension of the jet are denoted by ρ, μ and γ, respectively.

The behaviour of the jet is analysed using the leading-order 1-D mass and momentum equations, derived by Eggers & Dupont (1994). The dimensionless form of the equations, obtained by choosing $\bar{h}_0$ as the characteristic length scale, the inertial time $\tau_i = (\rho \bar{h}_0^3/\gamma)^{1/2}$ as the characteristic time scale and $\gamma/\bar{h}_0^2$ as the pressure scale, are written as

$$\frac{\partial h}{\partial t} = -\frac{1}{2h}\frac{\partial}{\partial z}(h^2 u), \tag{2.1a}$$

$$\frac{\partial u}{\partial t} = -u\frac{\partial u}{\partial z} - \frac{\partial p}{\partial z} + 3Oh_{in}\left(2\frac{\partial h}{\partial z}\frac{\partial u}{\partial z}\frac{1}{h} + \frac{\partial^2 u}{\partial z^2}\right) + Bo_{in}, \tag{2.1b}$$

where the dimensionless pressure $p(z, t)$ is expressed as

$$p = \left(\frac{1}{h\left[1+\left(\dfrac{\partial h}{\partial z}\right)^2\right]^{1/2}} - \frac{\dfrac{\partial^2 h}{\partial z^2}}{\left[1+\left(\dfrac{\partial h}{\partial z}\right)^2\right]^{3/2}}\right). \tag{2.2}$$

In (2.1), $h(z, t)$ and $u(z, t)$ represent the radius of the jet interface and the velocity at the axial distance z. The system of equations (2.1) are governed by the dimensionless Ohnesorge (Oh_{in}) and Bond (Bo_{in}) numbers defined at the inlet. The Ohnesorge number, expressed as $Oh_{in} = \mu/(\rho\gamma\bar{h}_0)^{1/2}$, relates the viscous forces to inertial and surface tension forces. The Bond (Eötvös) number, denoted by $Bo_{in} = \rho g\bar{h}_0^2/\gamma$, measures the strength of the surface tension forces to body forces. A high Oh_{in} or Bo_{in} leads to a stabilised jet interface, thus increasing the stability of the base flow.

Using the associated characteristic velocity $\bar{h}_0/\tau_i$, the non-dimensional boundary conditions for the jet at nozzle inlet are reduced to

$$h(0, t) = 1, \tag{2.3a}$$

$$u(0, t) = \sqrt{We_{in}}. \tag{2.3b}$$

Here, We_{in} represents the Weber number defined at the nozzle inlet, $We_{in} = \rho \bar{h}_0 \bar{u}_0^2/\gamma$, and measures the ratio between the kinetic energy and the surface energy.

The steady-state form of the continuity equation (2.1*a*) gives the relation between the steady-state shape h_b and velocity u_b as

$$h_b^2 u_b = Q = \sqrt{We_{in}}, \tag{2.4}$$

where Q is the dimensionless flow rate, obtained from the nozzle conditions. This gives $u_b = \sqrt{We_{in}}/h_b^2$. Using the relation (2.4), the steady-state momentum equation (2.1*b*) reduces to

$$2Q^2 h_b' - h_b^5 C' + 6QOh_{in}(h_b h_b'^2 - h_b^2 h_b'') + h_b^5 Bo_{in} = 0, \tag{2.5}$$

where derivatives are with respect to z and C is the jet interfacial curvature, expressed as

$$-h_b^2 C' = \frac{h_b'}{[1 + (h_b')^2]^{1/2}} + \frac{h_b h_b' h_b'' + h_b^2 h_b'''}{[1 + (h_b')^2]^{3/2}} - \frac{3h_b^2 h_b' (h_b'')^2}{[1 + (h_b')^2]^{5/2}}. \tag{2.6}$$

For the fixed nozzle inlet, equation (2.5) is subject to boundary condition $h_b = 1$ at $z = 0$. Two more boundary conditions are needed to well define this differential problem of order three. However, exempting the jet tip from the base flow calculation gives us the liberty to impose a constant slope ($h_b' = 0$) and curvature ($h_b'' = 0$) at the exit of the jet. It should be noted that the boundary conditions applied at the jet exit should be treated as a way to close the differential problem rather than depicting physical boundary conditions. We made sure that these boundary conditions did not impact the overall base-state solution by computing the solution over a large enough domain where the base-state solution naturally converges to a solution with $h_b' = 0$ and $h_b'' = 0$.

3. Nonlinear simulations

The strength of a nonlinear simulation lies in its ability to capture the exact response of the jet interface, including the shape close to the breakup point where the interface radius h approaches a zero value. Often, the external forcing does not result in the breakup of fixed-sized drops; rather the regular-sized drops are followed by much smaller 'satellite drops'.

Keeping this in view, we analyse the response of the jet in the presence of an external forcing. We aim to find the optimal forcing that results in the most unstable jet. The breakup length, which is the length of the stable jet between the nozzle and the breakup point, is chosen as the quantifier to compare the effect of different forcings, with the optimal forcing resulting in the shortest possible breakup length.

We begin with the description of the modified nonlinear governing equations used for the simulations, followed by the numerical scheme implemented to capture jet breakup. Finally, we present the comparison of breakup characteristics of the jet for different inlet forcings.

3.1. *Governing equations*

In order to remove the singularity in expression (2.2) for the pressure, when $h(z, t) \to 0$, we define the interface radius $h(z, t)$ in terms of the function $a(z, t)$ where $a = h^2$. The governing equations (2.1) thus transform into

$$\frac{\partial a}{\partial t} = -\frac{\partial}{\partial z}(au), \tag{3.1a}$$

$$\frac{\partial u}{\partial t} = -u\frac{\partial u}{\partial z} - \frac{\partial p}{\partial z} + 3Oh_{in}\left(\frac{\partial}{\partial z}\left(a\frac{\partial u}{\partial z}\right)\frac{1}{a}\right) + Bo_{in}, \tag{3.1b}$$

$$p = \left(\frac{\left(2 - \dfrac{\partial^2 a}{\partial z^2}\right)a + \left(\dfrac{\partial a}{\partial z}\right)^2}{2\left(\dfrac{1}{4}\left(\dfrac{\partial a}{\partial z}\right)^2 + a\right)^{3/2}}\right). \tag{3.1c}$$

The base-state solution for the jet interface ($a_b = h_b^2$) is obtained by solving (2.5). We model the external forcing on the jet by perturbing only the inlet velocity using a forcing of the form

$$u_f(0, t) = \mathrm{Re}(\epsilon \mathrm{e}^{\mathrm{i}\omega t}), \tag{3.2}$$

where ϵ represents the amplitude of the forcing and ω represents the angular forcing frequency. In the presence of the forcing, the boundary conditions at the inlet are modified to $a(0, t) = 1$ and $u(0, t) = \sqrt{We_{in}} + u_f$. No boundary conditions are defined at the other extremity of the domain close to the tip. Nonetheless, a special treatment is applied for the tip, as explained in the next section.

3.2. *Numerical scheme*

The governing equations (3.1) are first discretised in space, after which the resulting ordinary differential equations (ODEs) are integrated in time. Diffusion terms are evaluated using second-order finite differences, with a central scheme for intermediate nodes and a forward or backward scheme for boundary nodes. Advection terms are obtained using a weighted upwind scheme inspired by Spalding's (1972) hybrid difference scheme. Unlike the latter, which approximates the convective derivative using a combination of central and upwind schemes, we evaluate the derivative based on a combination of forward and backward finite differences. An advection term $\mathrm{d}A/\mathrm{d}z$ is evaluated at node i as

$$\left(\frac{\mathrm{d}A}{\mathrm{d}z}\right)_i = \beta\left(\frac{\mathrm{d}A}{\mathrm{d}z}\right)_{i,b} + (1 - \beta)\left(\frac{\mathrm{d}A}{\mathrm{d}z}\right)_{i,f}, \tag{3.3}$$

where indices b and f refer to the backward and forward finite difference schemes, and β is a weight coefficient that depends on the local value of velocity u at node i together with a parameter α:

$$\beta = \frac{\tanh(\alpha u_i) + 1}{2}. \tag{3.4}$$

For the range of feed velocities considered in this study, numerical stability was always ensured by using a 10-point stencil. Thus, the backward difference term relies

on a stencil that spans nodes $i-5$ to $i+4$, and the forward difference term employs nodes $i-4$ to $i+5$. For large enough downstream or upstream velocities, β will tend to 1 or 0, respectively; hence (3.3) reduces to a regular upwind difference scheme. For smaller velocity magnitudes in between, (3.3) produces a weighted combination of backward and forward differences. In our simulations, we choose $\alpha = 50$ so that the transition between the backward and forward difference schemes mostly occurs when $|u| < 0.05$. Finally, advection terms at nodes close to the boundary are evaluated based on the values of the closest nine adjoining nodes.

After obtaining all spatial derivatives, the resulting ODEs are integrated using the MATLAB solver `ode23tb`, which implements a trapezoidal rule and a backward differentiation formula known as TR-BDF2 (Bank *et al.* 1985), and uses a variable time step to reduce the overall simulation time.

The numerical domain L is taken sufficiently large to capture the breakup of the jet. The jet interface is initialised by the solution of (2.5) obtained numerically with the MATLAB `bvp4c` solver. The corresponding velocity at each axial location is then obtained by equating the interface radius with the constant inlet flow rate Q. The validation of the numerically obtained base-state solution for the jet interface is presented in § A.1. It should be noted that the jet is initialised only for a segment of the domain L with the steady-state equation. For the remaining segment of the domain, both the jet radius and its velocity are initialised to zero. Defining the initial conditions with the base-state solution only for a part of the domain L helps to reduce the computational cost without any loss in the accuracy of the results obtained. The axial span of the base-state solution does not affect the quasi-steady jet characteristics, which are the focal point of our numerical analysis. A validation for the same is presented in § A.2.

At every time step, the solution is evaluated for three conditions:

(i) Pinch-off (breakup). This is defined as when the value of a passes below a threshold value of 10^{-5}. The corresponding time t_{po} is saved and the position of the jet tip is updated as $N_{tip} = N_{po}$, where N_{po} is the pinch-off location. The solution for a and u beyond N_{tip} is set to zero. For subsequent time steps, N_{tip} has two possibilities – it can either advance or recede, which requires the following two conditions.

(ii) Advancing jet. The values of a at nodes $N_{tip}-1$ and N_{tip} are extrapolated to find a at $N_{tip}+1$. If the extrapolated value is larger than a predefined value of 5×10^{-3}, the parameter N_{tip} is incremented by 1, and a and u at the new N_{tip} are assigned values extrapolated from its previous two neighbours.

(iii) Receding jet. If the value of f at N_{tip} falls below a predefined value of 10^{-3}, a and u at N_{tip} are set to zero and the parameter N_{tip} is reduced by 1.

These three conditions enable the numerical integration of the governing equations in a way that captures accurately the breakup of the jet and the motion of the tip. A validation of the numerical scheme is presented in § A.3.

3.3. *Nonlinear simulation results*

Using the numerical scheme presented in the previous section, nonlinear simulations were performed for a jet governed by (3.1) for fixed inlet characteristics: $Oh_{in} = 0.3$, $We_{in} = 1.75$ and $Bo_{in} = 0.1$. The jet inlet velocity is subjected to time-harmonic forcing of the form given by (3.2) with a fixed amplitude ϵ and for forcing frequency $\omega = [0.4 - 3.2]$.

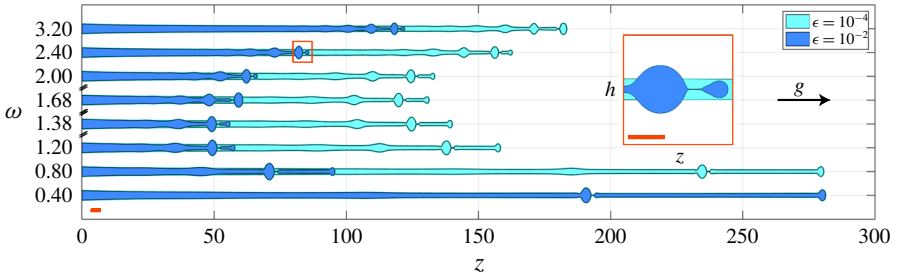

FIGURE 1. The jet intact shape along the axial direction z for a gravity jet defined by $Oh_{in} = 0.3$, $Bo_{in} = 0.1$ and $We_{in} = 1.75$ and perturbed by different inlet forcing frequencies ω and forcing amplitudes $\epsilon = 10^{-2}$ and $\epsilon = 10^{-4}$. For clarity, only the shape corresponding to the shortest breakup length for every frequency is plotted. The forcing frequencies are in steps of $\delta = 0.4$ except for certain intermediate ranges highlighted by the axis break symbol. The jets of two different colours represent the shape at the same forcing frequency but different forcing amplitudes ϵ. We see that for $\epsilon = 10^{-2}$ the breakup length is the minimum for $\omega = 1.38$ and for $\epsilon = 10^{-4}$ it is minimum for $\omega = 1.68$. The box in red shows the zoomed image of the jet close to a breakup, highlighting the existence of a satellite and a main drop. The zoomed image has radial h and axial z dimensions drawn to the same scale, each representing a dimensionless size of 6. The red bar in both the plots represents a dimensionless radial length scale of 2, which is also the size of the dimensionless nozzle diameter.

The simulations were run for a sufficiently long time to enter a permanent regime wherein the jet breaks up at regular intervals of time and at fixed axial location. In the quasi-steady regime, the breakup period ΔT_{po} is defined as the time difference between two consecutive breakups or pinch-offs and the breakup length l_c as the stable length of the jet between the nozzle and the pinch-off location. We use l_c as the quantifier to determine the stability of the jet to external forcing such that the most amplified disturbance caused by the optimal frequency ω_{opt} will compel the jet to have the shortest possible breakup length.

We begin our analysis for fixed amplitudes $\epsilon = 10^{-2}$ and $\epsilon = 10^{-4}$. The response of the jet due to different forcing frequency ω in the permanent regime for the two above-mentioned amplitudes can be seen in figure 1. Jets enforced by the same disturbance amplitude at the inlet are represented by the same colour. For visual clarity we plot the response only for certain frequencies and for the jet shape pertaining to the shortest breakup length. First, figure 1 clearly shows the existence of a main drop and a satellite drop for all the frequencies. Second, for $\epsilon = 10^{-2}$ we conclude that the optimal forcing frequency is $\omega_{opt} = 1.38$ because it manifests the jet to have the shortest l_c. Third, and most strikingly, we notice that for a lower forcing amplitude of $\epsilon = 10^{-4}$, the optimal forcing increases to $\omega_{opt} = 1.68$. We would like to highlight here that a similar inverse relation between the forcing amplitude and the optimal forcing frequency for gravitationally stretched jets can also be observed through the linear response analysis results presented in Consoli-Lizzi *et al.* (2014) and Consoli-Lizzi (2016). Finally, at all forcing frequencies, the breakup length for the jet with $\epsilon = 10^{-4}$ is always larger than for $\epsilon = 10^{-2}$.

To investigate further the breakup characteristics for the amplitudes $\epsilon = 10^{-2}$ and $\epsilon = 10^{-4}$ due to ω_{opt}, we plot the interface evolution in the permanent regime as shown in figures 2(*a*) and 2(*c*), where regular-sized main drop formation is followed

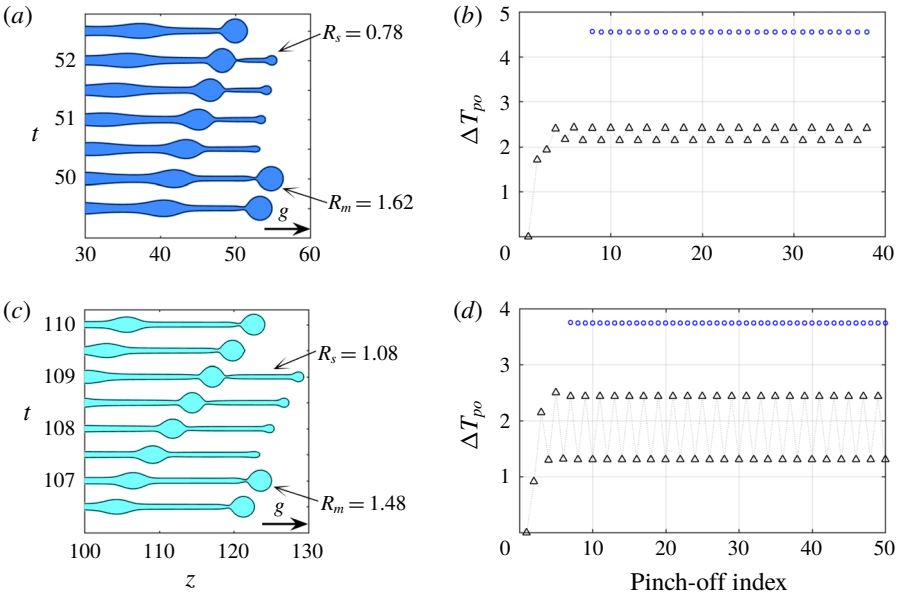

FIGURE 2. Breakup characteristics for a gravity jet defined by $Oh_{in} = 0.3$, $Bo_{in} = 0.1$ and $We_{in} = 1.75$ and perturbed with ω_{opt}. Panels (a,b) correspond to a forcing with $\epsilon = 10^{-2}$ and $\omega_{opt} = 1.38$; and panels (c,d) refer to a forcing with $\epsilon = 10^{-4}$ and $\omega_{opt} = 1.68$. In panels (a,c) is elaborated the interface profile at the time of breakup with the existence of a satellite drop after the main drop is released. The main and satellite drop radii for both the cases have been highlighted. The axial and radial dimensions of (a,c) represent the same length scale. In panels (b,d) is represented the breakup period ΔT_{po}. The black triangles refer to ΔT_{po} between consecutive drops and the blue circles represent that between two consecutive main (or satellite) drops. The breakup frequency ω_{po} is equal to 1.38 and 1.68 in (b,d) respectively.

by the release of a satellite drop. For both the amplitudes, we see a distinct difference between the main and satellite drop radii.

The breakup period ΔT_{po} resulting from the forcing imposed in figures 2(*a*) and 2(*c*) are plotted in figures 2(*b*) and 2(*d*), respectively, where the black triangles represent the ΔT_{po} obtained for two consecutive pinch-offs whereas the blue circles denote ΔT_{po} obtained for two consecutive main (or satellite) drop pinch-offs. The latter is observed to be the same for the main and satellite drop formation (as shown in blue circles). However, the time of formation of a satellite drop does not lie exactly midway between the time of formation of the main drops and *vice versa*. This results in obtaining two oscillating breakup periods (as shown by the black triangles). We further observe that the frequency of breakup ($\omega_{po} = 2\pi/\Delta T_{po}$) obtained using the breakup period for consecutive main (or satellite) drops responds to the externally applied forcing at the jet inlet. For forcing amplitudes $\epsilon = 10^{-2}$ and 10^{-4}, $\omega_{po} = 1.38$ and 1.68, respectively.

Finally, for the constant flow rate of the jet, the breakup period related to the consecutive pinch-offs is used to obtain the drop radius for the satellite and main drops. Note here that the definition of the main and satellite drop radii coincide with the classical definition of volume-equivalent radii. We notice that, at the optimal forcing frequency, the main drop radius R_m decreases from 1.62 to 1.48 dimensionless

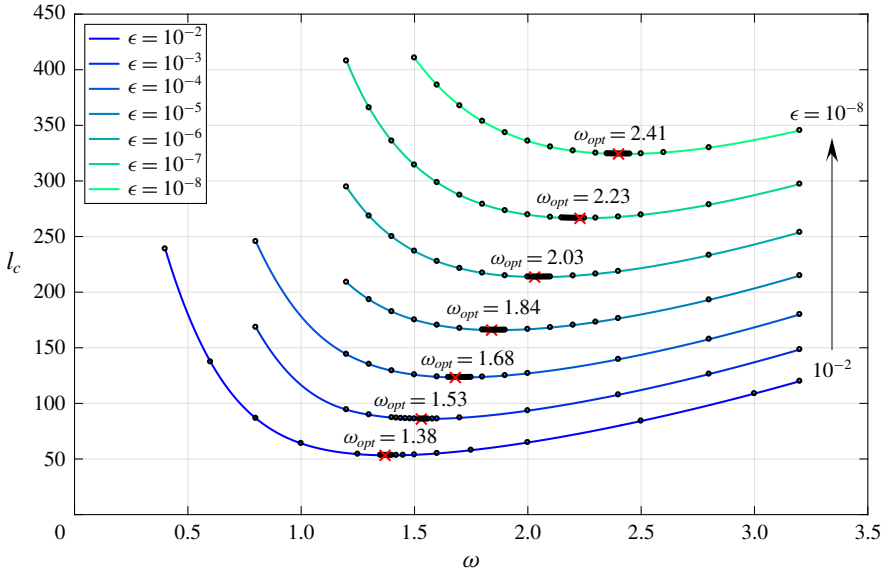

FIGURE 3. The breakup length l_c as a function of forcing frequency ω for a gravity jet defined by $Oh_{in} = 0.3$, $Bo_{in} = 0.1$ and $We_{in} = 1.75$. Each curve is indicative of a fixed forcing amplitude ϵ. For a fixed ϵ, the optimal forcing frequency related to the shortest l_c is represented by a red cross. We observe that the optimal frequency increases as ϵ decreases and does not appear to saturate even for lower amplitudes of 10^{-8}. The black circles represent the data from numerical simulations.

units as ϵ reduces from 10^{-2} to 10^{-4}. On the contrary, the satellite drop radius R_s increases from 0.78 to 1.08 dimensionless units for $\epsilon = 10^{-2}$ and $\epsilon = 10^{-4}$, respectively. The longer intact jet length obtained for lower forcing amplitude $\epsilon = 10^{-4}$ results in a larger downstream velocity close to the tip due to the presence of gravity. Eventually, it results in the formation of highly stretched satellite drops in comparison to the ones obtained for lower amplitude of $\epsilon = 10^{-2}$ as seen in figure 2(*a*,*c*).

We now return to the most salient feature observed in figure 1, where the optimal forcing frequency ω_{opt} increased with a decrease in forcing amplitude. To explore if this effect existed for smaller amplitudes, we simulated the same system for different forcing amplitudes $\epsilon = [10^{-2}$–$10^{-8}]$, and plotted the breakup length l_c as a function of the forcing frequency ω as shown in figure 3, where the optimal forcing frequency for a fixed ϵ is marked with a red cross. The results show an increase in l_c and ω_{opt} as ϵ decreases, which is in qualitative agreement with the linear response analysis results presented in Consoli-Lizzi (2016). The increase in breakup length is obvious due to the decreasing destabilising strength of the forcing amplitude. The increase in optimal forcing frequency, however, is the most interesting observation drawn from the numerical results, since it is expected to saturate for small enough forcing amplitudes. The increase in ω_{opt} as ϵ decreases from 10^{-2} to 10^{-8} is a consequence of the stretched base state due to gravity, which results in the downstream stretching of the perturbation wavelength initiated at the nozzle. As the forcing amplitude decreases, the stable jet length l_c increases and so does the stretching close to the jet tip. Thus to compensate for the larger stretching, the breakup potential of the forcing is sustained by increasing the forcing frequency.

To conclude, the numerical simulations confirm the dependence of ω_{opt} on the forcing amplitude, a factor generally neglected for linear stability analysis as long as $\epsilon \ll 1$. The trend also constitutes a major difference from a jet with no gravity effect ($Bo_{in} = 0$), where ω_{opt} is independent of ϵ (see figure 20 in § A.4). Finally, we confirm that the preferred-mode analysis carried out for the jet is solely due to the effect of external forcing. For the given parameter range, the jet tip did not induce any self-sustained breakups.

4. Local stability analysis

The linear stability theory is applicable for small forcing amplitudes ($\epsilon \ll 1$) and does not take into account its absolute value, a parameter that has already been shown in § 3.3 to influence the optimal forcing frequency. Nevertheless, we begin our analysis in the local framework by first obtaining the dispersion relation for parallel viscous jets in the absence of gravity, which is used as a basis for obtaining the absolute–convective instability transition criteria in § 4.2. Next, the dispersion relation for parallel jets is suitably modified to include the spatial variation of the gravitationally stretched base flow and the spatial stability of the jet is performed in § 4.3. Since the base state is spatially evolving, we extend our stability analysis using the WKBJ formulation in § 4.4.

4.1. *Local stability analysis for jets in the absence of gravity*

We derive the dispersion relation for the coupled equations (2.1), governing the growth of small perturbations about the base state. Considering the normal-mode expansion, the flow variables $h(z, t)$ and $u(z, t)$ are decomposed as

$$h(z, t) = h_b + \epsilon \hat{h} \mathrm{e}^{\mathrm{i}(kz-\omega t)}, \tag{4.1a}$$

$$u(z, t) = u_b + \epsilon \hat{u} \mathrm{e}^{\mathrm{i}(kz-\omega t)}, \tag{4.1b}$$

where $\epsilon \ll 1$, with $\hat{h}$ and $\hat{u}$ as complex constants, and where k and ω are, respectively, the dimensionless spatial wavenumber and the temporal frequency, which may both be complex. Similarly, for the variable representing the square of interface, $a(z, t)$ is decomposed as

$$a(z, t) = a_b + \epsilon \hat{a} \mathrm{e}^{\mathrm{i}(kz-\omega t)}, \tag{4.2}$$

where $a_b = h_b^2$ and $\hat{a} = 2h_b\hat{h}$. Inserting the above expansion into (2.1), linearising about (h_b, u_b) and replacing $h^2 \to a$ will lead to a linearised system of equations, which can be formulated as an eigenvalue problem with the eigenmodes represented by $\hat{\boldsymbol{q}} = [\hat{a}, \hat{u}]$.

In the absence of gravity, $\hat{\boldsymbol{q}}$ represents a constant independent of z, $u_b = \sqrt{We}$ and $h_b = 1$. Combining both the linearised continuity and momentum equations leads to the dispersion relation

$$\omega = \sqrt{We}\, k - \frac{3\mathrm{i}Ohk^2}{2} \pm \mathrm{i}\sqrt{\frac{(k^2 - k^4)}{2} + \frac{9Oh^2k^4}{4}}, \tag{4.3}$$

where Oh is constant throughout the domain. The dispersion relation is used to perform a spatio-temporal stability analysis, which includes the effect of advection speed of the jet on its stability properties. In this framework, we define the impulse response of a system to a localised perturbation that generates a wavepacket growing in space and time. In the laboratory framework, the spatio-temporal behaviour of

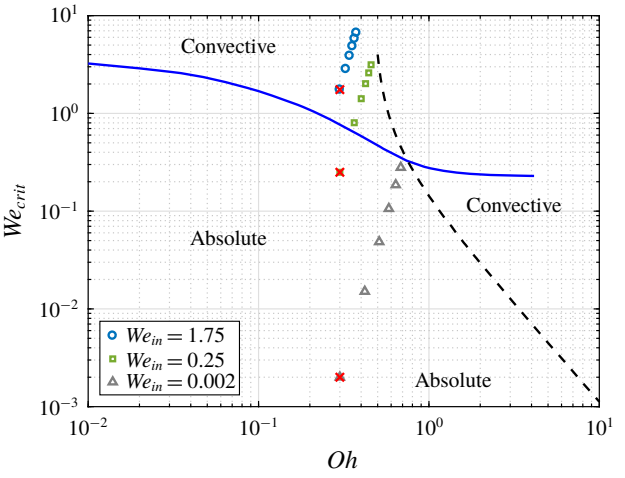

FIGURE 4. The absolute–convective transition (represented by full and dashed lines) for viscous jets ($Bo_{in} = 0$). The local variation in Oh_z and We_z for three jets with different We_{in} (constant $Oh_{in} = 0.3$, $Bo_{in} = 0.1$, $L = 50$) are plotted with different markers, where the red cross for each represents the inlet condition at $z = 0$. The distance between consecutive markers for the same jet represents an axial gap of 10 units.

the wavepacket can be described in terms of the complex absolute wavenumber k_0 and the corresponding complex absolute frequency $\omega_0 = \omega(k_0)$ whose imaginary part $\omega_{0,i}$ will determine the temporal evolution of the wavepacket. For $\omega_{0,i} > 0$ the system is absolutely unstable since the disturbance grows fast enough to invade the entire domain in the laboratory frame; and for $\omega_{0,i} < 0$ the system is convectively unstable as the localised perturbations are allowed to convect downstream before they grow in the laboratory frame. The complex pair (k_0, ω_0) is defined using the saddle point condition or the Briggs–Bers zero-group-velocity criterion, together with the dispersion relation

$$\frac{\mathrm{d}\Delta(\omega_0, k_0)}{\mathrm{d}k} = 0, \quad \Delta(\omega_0, k_0) = 0, \tag{4.4}$$

where Δ represents the dispersion relation (4.3) and

$$\frac{\partial \Delta}{\partial k} = \sqrt{We} - 3\mathrm{i}Ohk \pm \mathrm{i}\frac{1 - 2k^2 + (3Ohk)^2}{\sqrt{2(1-k^2) + (3Ohk)^2}}. \tag{4.5}$$

Equation (4.4) identifies the critical dimensionless speed We_{crit}, for a fixed Oh, which signifies the transition of the jet from an absolutely unstable to a convectively unstable system as shown in figure 4 with the full and dashed lines. The two curves are obtained for a system initialised either using a low or a high Oh, respectively. For the intermediate values of Oh, we obtain two saddle points, thus giving two distinct values of the critical curve.

4.2. *Local stability analysis for jets in the presence of gravity*

Extending the formalism for parallel jets to spatially varying jets, we derive the dispersion relation for the coupled equations (2.1), governing the growth of small

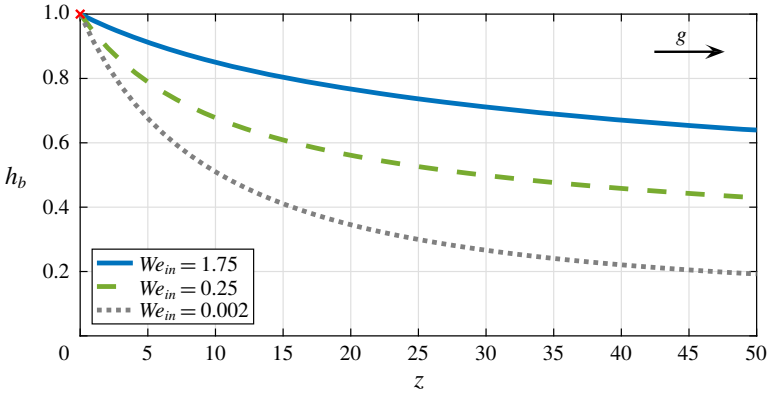

FIGURE 5. The stretching (or necking) close to the nozzle of the base flow due to the presence of gravity for a jet with $Oh_{in} = 0.3$, $Bo_{in} = 0.1$ and three different We_{in}. Clearly, the effect of gravity is prominent for the jet with the smallest We_{in}.

perturbations about the base state. The linearised system of equations obtained around the spatially varying base flow can be formulated as an eigenvalue problem with the eigenmodes represented by $\hat{\boldsymbol{q}}(z) = [\hat{a}(z), \hat{u}(z)]$ as functions of z. Next we express the local stability of a gravity jet by introducing the terms Oh_z and We_z, which are the local dimensionless numbers at an axial distance of z from the nozzle. They are expressed as

$$Oh_z = Oh_{in}\sqrt{\frac{h_b(0)}{h_b(z)}}, \tag{4.6a}$$

$$We_z = h_b(z)u_b^2(z). \tag{4.6b}$$

We then plot the values Oh_z and We_z along the entire axial domain L above the absolute–convective transition curve in figure 4. The variation in local Oh_z and We_z along the jet defined within a domain size $L = 50$ for $Oh_{in} = 0.3$ and $Bo_{in} = 0.1$ and for three different inlet Weber numbers $We_{in} = [1.75, 0.25, 0.002]$ are represented by the different markers in figure 4. The gap between consecutive markers is representative of an axial interval of 10 units. In each case, the red cross represents the inlet of the jet whose base state is shown in figure 5. We remind the reader that the case with $We_{in} = 1.75$ corresponds to the jet whose numerical analysis has been presented in § 3.3.

For $We_{in} = 1.75$ and 0.002, the entire jet exists in the convective and absolute region, respectively. For intermediate $We_{in} = 0.25$, there exists a small pocket of absolute instability close to the nozzle, after which the local parameters modify along the downstream direction, resulting in the transfer of the jet into a convectively unstable regime.

The parameter Bo_{in} indirectly affects the instability of the jet through the base-state solution. Since Bo_{in} is constant, its relative strength for the stretching of the jet interface depends on the corresponding value of We_{in}, with the effect being more pronounced for lower values of We_{in} as shown in figure 5.

Next, for the spatially varying base flow, we perform the stability analysis in a local framework wherein the system is considered parallel at each axial location. The local

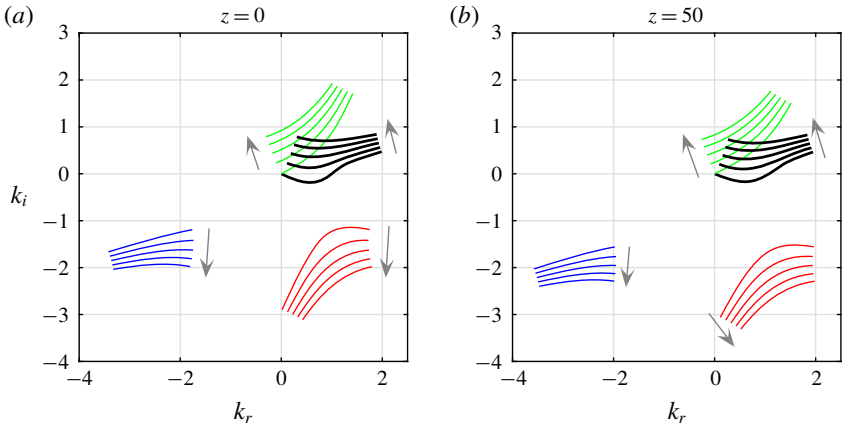

FIGURE 6. The four k branches shown in four different colours, obtained as a solution of the dispersion relation for complex ω and for increasing values of ω_i for a jet defined by $Oh_{in} = 0.3$, $Bo_{in} = 0.1$ and $We_{in} = 1.75$ at (a) the nozzle outlet $z = 0$ and (b) the jet exit $z = L = 50$. The arrows represent the direction of movement of the waves for increasing values of ω_i.

dispersion relation, which now includes the local spatially varying base flow properties, is given by

$$\omega^2 - 2u_b(z)\omega k + \left(\frac{1}{2\sqrt{a_b(z)}} + u_b(z)^2 + 3\mathrm{i}Oh_z\omega\right)k^2 - 3\mathrm{i}Oh_z u_b(z)k^3 - \frac{\sqrt{a_b(z)}}{2}k^4 = 0. \tag{4.7}$$

For the convectively unstable jet ($We_{in} = 1.75$), the solution of the dispersion relation (4.7) for a given range of complex ω (with $\omega_i > 0$) results in obtaining four spatial branches, which are expressed as the roots of the fourth-order polynomial (4.7). The solution consists of upstream-propagating (denoted k^-) and downstream-propagating (denoted k^+) branches. To identify these branches, we successively add an artificial ω_i so as to separate the branches into the upper $k_i > 0$ and lower $k_i < 0$ planes (Huerre & Rossi 1998; Gallaire & Brun 2017). For a downstream-propagating k^+ branch damped in space, the associated $k_i > 0$. Based on this analysis, we obtain two downstream- and two upstream-propagating waves for the dispersion relation (4.7). The k branches for the localised dimensionless numbers at the nozzle inlet ($z = 0$) and domain end ($z = 50$) are shown in figure 6(a) and 6(b), respectively, with the two k^+ branches denoted by the black and green colours and the two k^- waves by the red and blue colours. The presence of two k^+ and k^- waves is not specific to the present jet characteristics but rather exists for all the tested cases in the range of $Oh_{in} = [0.1,\ 10]$, $We_{in} = [0.8,\ 10]$ and $Bo_{in} = [0,\ 1]$ for $L = 50$.

4.3. *Spatial stability analysis*

Since the base flow with $We_{in} = 1.75$ exists in the convectively unstable regime (see figure 4), we then proceed to analyse the base flow using the spatial stability framework, wherein the spatial growth rate for the imposed real frequency determines the flow stability.

Given the polynomial nature of the dispersion relation, there are four spatial waves. We have verified that two of them are k^+, downstream-propagating, waves while the remaining two are k^-, upstream-propagating, waves (see figure 6). For a more detailed

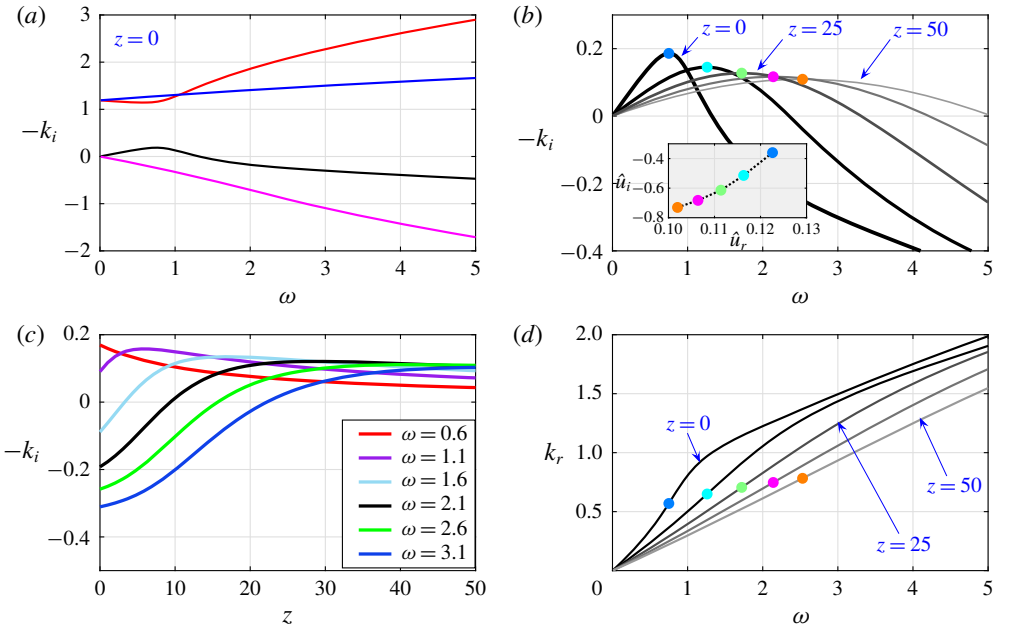

FIGURE 7. (*a*) Growth rate $-k_i$ for a jet defined by $Oh_{in} = 0.3$, $Bo_{in} = 0.1$ and $We_{in} = 1.75$, plotted as a function of the frequency for the four k branches at the nozzle exit with the dominant k branch represented in black. (*b*) The growth rate corresponding to the dominant k branch at different axial locations. The inset shows the evolution of the locus of the real and imaginary parts of $\hat{u}_r$ and $\hat{u}_i$ at the optimal frequency as z increases. (*c*) The growth rate $-k_i$ of the dominant k branch as a function of z for various ω. (*d*) The k_r related to the optimal growth rate in (*b*) as a function of real frequency. The coloured markers (●) in (*b*) and (*d*) correspond to the same forcing frequency and the axial location.

account on the nature of spatial waves in capillary jets, depending on the flow model, the reader is referred to Guerrero, González & García (2016).

Among the four k waves, only one of the k^+ waves is seen to be amplified. To obtain this dominant k wave, we plot the spatial growth rate $-k_i$ as a function of the real forcing frequency ω at the nozzle inlet. As shown in figure 7(*a*), among the four k branches, only the branch denoted in black has a growth rate that is positive in its propagation direction. We chose the k wave corresponding to this amplified k^+ branch as the dominant wavenumber for all frequencies. The relevant $k(z)$ branches are then obtained for different z along the jet as shown in figure 7(*b*,*d*) by imposing the spatially dependent base flow and Oh_z in (4.7). Figure 7(*b*) shows that the most amplified frequency shifts to higher values as one travels away from the nozzle. The associated eigenmode $\hat{\boldsymbol{q}}(z)$ also changes as one progresses downstream. Imposing $\|\hat{\boldsymbol{q}}\| = 1$ at every axial location as the normalisation condition, together with $\hat{a}_i = 0$ to set the phase, we see in figure 7(*c*) the evolution of the locus of the real and imaginary parts of the remaining degrees of freedom $\hat{u}_r$ and $\hat{u}_i$ as z increases (remember that $\hat{u}_r^2 + \hat{u}_i^2 + \hat{a}_r^2 = 1$). While this locus is difficult to interpret from a physical point of view, it highlights the change of the eigenmode along the jet axis in such non-parallel gravity-driven jets.

The knowledge of the relevant k^+ wave obtained for a given ω allows us to evaluate the leading-order response due to different forcing frequencies imposed on the base

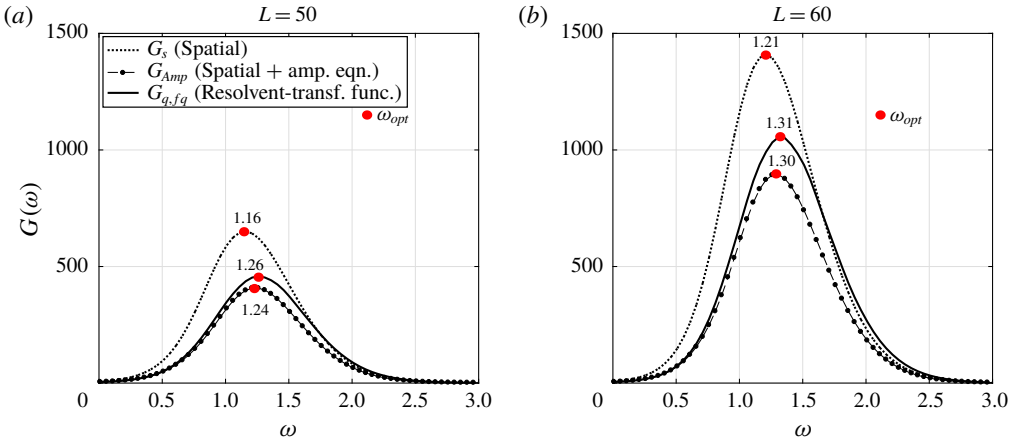

FIGURE 8. Comparison of the total gain G at different frequencies ω from the resolvent analysis and the spatial analysis for domain sizes (*a*) $L = 50$ and (*b*) $L = 60$ and for the jet defined by $Oh_{in} = 0.3$, $Bo_{in} = 0.1$ and $We_{in} = 1.75$. The resolvent gain is computed by using the transfer function and the direct mode obtained from the spatial analysis. All the theories predict a shift in ω_{opt} as L is increased.

flow, conveniently expressed as

$$\boldsymbol{q}'(z, t) = \hat{\boldsymbol{q}}(\omega, z) \exp\left[\mathrm{i}\left(\int_0^z k(\omega, z')\,\mathrm{d}z' - \omega t\right)\right]. \tag{4.8}$$

The overall response norm defined in a domain size L is then given as

$$G_s(\omega, L) = \left\| \int_0^L \hat{\boldsymbol{q}}(\omega, z) \exp\left[\mathrm{i}\left(\int_0^z k(\omega, z')\,\mathrm{d}z' - \omega t\right)\right] \right\|. \tag{4.9}$$

This allows us to determine the optimal forcing frequency ω_{opt} that results in the maximal gain

$$G_{s,max}(L) = \max_{\omega} [G_s(\omega, L)], \tag{4.10}$$

attained at a frequency ω_{opt}. Figure 8 (in dotted lines) shows the spatial gain as a function of forcing frequency for two arbitrary domain sizes $L = 50$ and 60. We notice that ω_{opt} shifts from 1.16 to 1.21 as we increase the domain size.

4.4. *Weakly non-parallel stability analysis (WKBJ)*

In order to further incorporate the non-parallelism of the base flow, we extend our spatial analysis by including the WKBJ formalism introduced by Gaster *et al.* (1985) and Huerre & Rossi (1998) for a spatial mixing layer and applied by Viola *et al.* (2016) for swirling flows.

In this framework, we introduce a slow streamwise scale Z, which relates to the fast scale z as $Z = \eta z$, where $\eta \ll 1$ is a measure of the weak non-parallelism. The new base flow depends only on Z and the global response to inlet forcing takes the modulated wave form

$$\boldsymbol{q}'(Z, t) \sim A(Z)\hat{\boldsymbol{q}}(Z, 0) \exp\left[\mathrm{i}\left(\frac{1}{\eta}\int_0^Z k(\omega, Z')\,\mathrm{d}Z' - \omega t\right)\right], \tag{4.11}$$

where $\hat{\boldsymbol{q}}(\omega, Z)$ is the local eigenmode and $k(\omega, Z)$ the local wavenumber at section Z and a fixed forcing frequency ω. The amplitude function $A(Z)$ acts as an envelope, smoothly connecting the progressive slices of the parallel spatial analysis. At each axial location, we impose $\hat{\boldsymbol{q}}^{\mathrm{H}} \cdot \hat{\boldsymbol{q}} = 1$, where $(\cdot)^{\mathrm{H}}$ is the transconjugate. As described in § A.6, imposing an asymptotic expansion and a compatibility condition, the local stability analysis is retrieved at zeroth order in η, while at first order in η the following amplitude equation is obtained:

$$M(Z)\frac{\mathrm{d}A(Z)}{\mathrm{d}Z} + N(Z)A(Z) = 0, \tag{4.12}$$

whose solution is given as

$$A(Z) = A_0 \exp\left(-\int_0^Z \frac{N(Z')}{M(Z')}\,\mathrm{d}Z'\right). \tag{4.13}$$

The functions $M(Z)$ and $N(Z)$ are defined in § A.6. The amplitude at the inlet is set as $A(0) = 1$, which simplifies the forcing expression at the inlet to $\boldsymbol{q}'(0, t) = \hat{\boldsymbol{q}}(0)\exp(\mathrm{i}\omega t)$. Finally, we express the total spatial gain at first order as

$$G^2_{Amp}(\omega, L) = \frac{\displaystyle\int_0^z A^{\mathrm{H}}(z')A(z')(\hat{\boldsymbol{q}}^{\mathrm{H}}(z') \cdot \hat{\boldsymbol{q}}(z'))\left[\exp\left(\int_0^{z'} -2k_i(z'')\,\mathrm{d}z''\right)\right]\mathrm{d}z'}{\hat{\boldsymbol{q}}^{\mathrm{H}}(0) \cdot \hat{\boldsymbol{q}}(0)}. \tag{4.14}$$

The global gain of the response due to the forcing frequency, for fixed domain sizes, is reported in figure 8, where $\omega_{opt} = 1.24$ and 1.30 for $L = 50$ and 60, respectively. The WKBJ approximation greatly modifies the gain when compared to the zeroth-order analysis and shifts the optimal forcing frequency predicted from the spatial analysis, which excludes the amplitude equation. However, to truly assess the validity of the amplitude equation, one needs to analyse the base flow in the global framework using the resolvent analysis, which will be the focus of our discussion in the next section.

5. Global stability analysis

Unlike the local stability analysis, the global stability framework allows taking into consideration the axially varying base state due to the stretching effect of gravity. The global stability analysis of the leading-order 1-D model was performed by Sauter & Buggisch (2005), and refined later on by Rubio-Rubio *et al.* (2013). Following the work of the previous authors, we first evaluate the inherent global stability of the base flow in § 5.1. We next perform a resolvent analysis in § 5.2 on the globally stable base flow to evaluate its response in the presence of a given perturbation.

5.1. *Global stability*

Since the base flow is spatially varying, the perturbations imposed on it are no longer sought in the form of Fourier modes but are expanded in the form

$$h(z, t) = h_b(z) + \epsilon\tilde{h}(z)\mathrm{e}^{\lambda t}, \tag{5.1a}$$

$$u(z, t) = u_b(z) + \epsilon\tilde{u}(z)\mathrm{e}^{\lambda t}, \tag{5.1b}$$

where $\epsilon \ll 1$, and $\tilde{h}(z)$ and $\tilde{u}(z)$ are the global stability modes related to the complex growth rate λ. Substituting expressions (5.1) in (2.1) and linearising around the base state (h_b, u_b) results in the general eigenvalue problem of the form

$$\lambda \boldsymbol{I} \begin{bmatrix} \tilde{h} \\ \tilde{u} \end{bmatrix} = \boldsymbol{M} \begin{bmatrix} \tilde{h} \\ \tilde{u} \end{bmatrix}, \tag{5.2}$$

with boundary conditions $\tilde{h}(0, t) = 0$ and $\tilde{u}(0, t) = 0$. We do not impose any boundary conditions at the end of the domain, $z = L$, since it is not possible *a priori* to distinguish between amplifying perturbations and transient disturbances. This will occur in any problem that involves an 'active system' and can support amplifying waves (Briggs 1964; Leib & Goldstein 1986). The global stability analysis presented in Rubio-Rubio *et al.* (2013) does not impose any boundary conditions for $z = L$ since the numerical method naturally converges to the most regular asymptotic solution of the base flow equation (2.5) and eigenvalue problem (5.2), as $z \to \infty$. Nonetheless, we checked that the dominant eigenvalue and eigenmode were unaffected by the presence of a Neumann boundary condition at $z = L$, namely $\mathrm{d}\tilde{u}(L)/\mathrm{d}z = 0$.

The complete expressions for the linear operator $\boldsymbol{M}$ can be found in § A.5. The solution of (5.2) results in a set of eigenmodes $(\tilde{h}, \tilde{u})$, whose growth rate and frequency are given by the real (λ_r) and imaginary (λ_i) parts of the related eigenvalue. A base state is stable to self-induced oscillations provided $\lambda_r < 0$.

To solve the eigenvalue problem, the Chebyshev collocation method is used to obtain the differential operators. Derivatives with respect to z are calculated using the standard Chebyshev differentiation matrices. Denoting the non-dimensional physical domain as L, the domain is mapped into the interval $-1 \leqslant y \leqslant 1$ by using the transformation $z = [(L/2) \times (y + 1)]$. The global stability scheme is validated against the results of Rubio-Rubio *et al.* (2013).

For the three cases of jets described in figure 5, with $L = 50$, $Oh_{in} = 0.3$, $Bo_{in} = 0.1$ and three different values of We_{in}, a global stability analysis is carried out using different resolutions ($N_1 = 100$, $N_2 = 125$, $N_3 = 150$) to exclude spurious eigenvalues. The eigenvalue spectra for $We_{in} = 0.25$, 1.75 and 0.002 are represented in figures 9(*a*), 9(*c*) and 10(*a*), respectively. The dominant eigenvalues have $\lambda_r < 0$ (for $We_{in} = 0.25$ and 1.75) and $\lambda_r > 0$ (for $We_{in} = 0.0025$), thus representing globally stable and unstable jets, respectively. Note, however, that the local stability analysis of the globally stable flow with $We_{in} = 0.25$ predicts the jet to have a small 'pocket' of absolute instability close to the nozzle.

Eigenmodes corresponding to the dominant eigenvalues are presented in the accompanying figures. We note that the dominant eigenmode, as represented in figures 9(*b*), 9(*d*) and 10(*b*), has an amplitude that grows downstream. Figure 10(*b*) also shows that the wavelength grows downstream. This is a consequence of the fluid acceleration caused by gravity (Tomotika 1936; Rubio-Rubio *et al.* 2013) and can be interpreted from figure 7(*d*), where k_r is seen to decrease with increasing z for a fixed forcing frequency ω. Further we see that, close to the outlet, the eigenmodes evolve at a much larger length scale compared to that related to the variations in a steady-state jet, thus strengthening the argument that weakly non-parallel stability analysis should be used with care for predicting the global stability of the gravity jet. A similar warning for the use of local analysis under strong stretching is one of the main conclusions of the work presented in Rubio-Rubio *et al.* (2013).

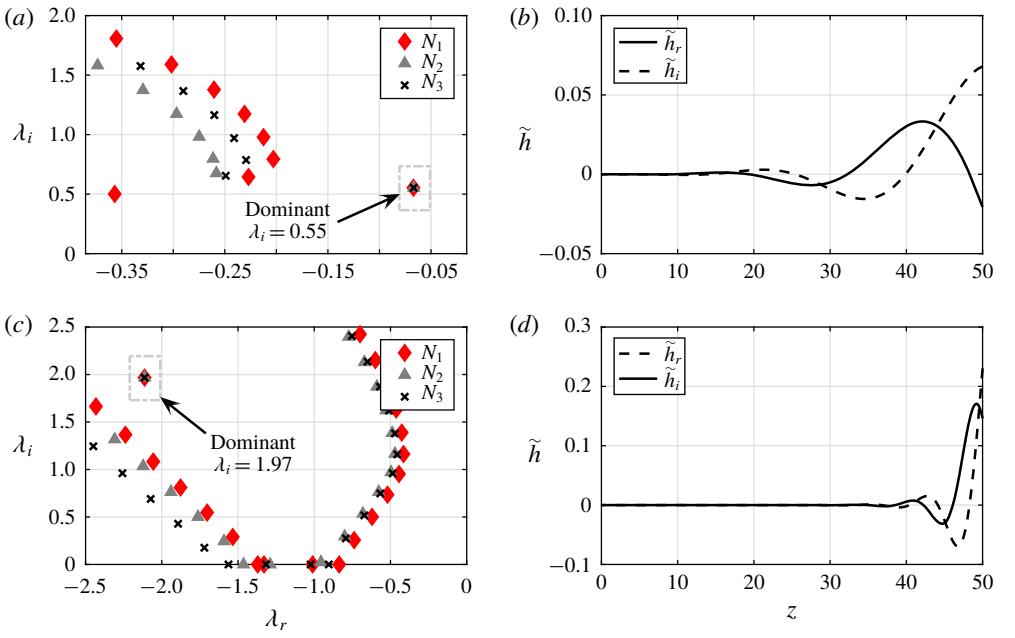

FIGURE 9. (*a*,*c*) Eigenvalue spectrum λ obtained for three different resolutions $N_1 = 100$, $N_2 = 125$ and $N_3 = 150$ and (*b*,*d*) the real and imaginary parts of the leading eigenfunction $\tilde{h}$, for $Oh_{in} = 0.3$, $Bo_{in} = 0.1$, $L = 50$ and evaluated for two different values of inlet Weber number. Panels (*a*,*b*) correspond to $We_{in} = 0.25$ where the leading eigenvalue has an eigenfrequency $\lambda_i = 0.55$. Panels (*c*,*d*) correspond to $We_{in} = 1.75$ with $\lambda_i = 1.97$. For both Weber numbers, the entire spectrum has $\lambda_r < 0$, rendering the system globally stable.

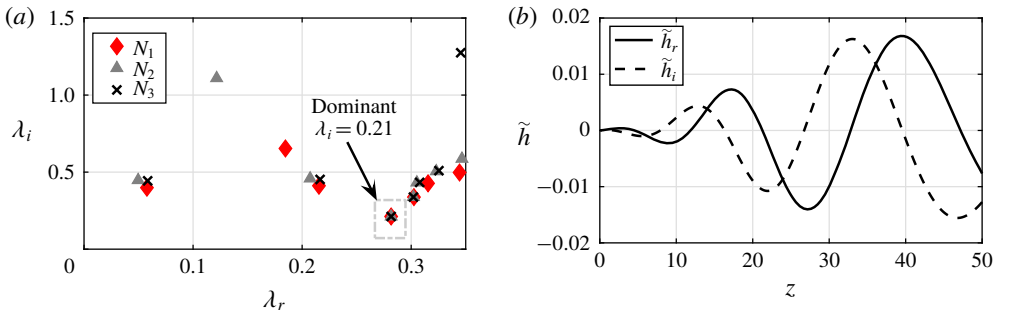

FIGURE 10. (*a*) Eigenvalue spectrum λ obtained for three different resolutions $N_1 = 100$, $N_2 = 125$ and $N_3 = 150$ and (*b*) the real and imaginary parts of the leading eigenfunction $\tilde{h}$, for $Oh_{in} = 0.3$, $Bo_{in} = 0.1$, $We_{in} = 0.002$ and $L = 50$. We note that the leading eigenvalue has a positive growth rate $\lambda_r > 0$, thus rendering the system globally unstable.

5.2. *Global resolvent*

Analysing the linear response of the base state for an external harmonic forcing at frequency ω is only well defined if the linear operator is stable, or, in other words, the base state is stable, where the imposed perturbations are allowed to travel

downstream before spreading in the entire domain under consideration. Otherwise the algebraically amplified solution is superimposed by the unforced naturally growing exponential mode. Keeping this in mind, in this section we present the resolvent analysis for the stable gravity jet ($We_{in} = 1.75$). We would like to remind the reader that a similar response analysis along the lines of the present work was presented in Consoli-Lizzi *et al.* (2014), and can also be found in Consoli-Lizzi (2016). To compare our linear resolvent results with the nonlinear simulations of § 3, we impose similar inlet forcing conditions and approximate the gain predicted by the resolvent analysis in terms of the forcing amplitude.

5.2.1. *Problem formulation*

The external force f is modelled as an incoming perturbation in the form of an unsteady upstream boundary condition of the 1-D Eggers and Dupont equations (2.1). The resulting linearised equation is represented as

$$\boldsymbol{I}\partial_t[\boldsymbol{s}] = \boldsymbol{M}[\boldsymbol{s}] + \boldsymbol{B}_f f, \tag{5.3}$$

where, as in the eigenvalue problem (5.2) with N as the resolution number, $\boldsymbol{s} = [h, u]$, $\boldsymbol{I}$ represents the identity matrix of rank $2N \times 2N$, $\boldsymbol{M}$ is the linear operator of rank $2N \times 2N$ (detailed in § A.5) and $\boldsymbol{B}_f$ is a $2N \times 2N$ prolongation operator that maps the inlet forcing f ($2N \times 1$) onto the bulk equation (Garnaud *et al.* 2013; Viola *et al.* 2016). Considering a time-harmonic forcing, $f = \tilde{f}\exp(-\mathrm{i}\omega t)$, results in an asymptotic flow response $\boldsymbol{s} = \tilde{\boldsymbol{s}}\exp(-\mathrm{i}\omega t)$ at the same frequency. Here $\tilde{\boldsymbol{s}} = [\tilde{h}, \tilde{u}]$. Imposing these transformations in (5.3) we obtain

$$-(\boldsymbol{M} + \mathrm{i}\omega\boldsymbol{I})\tilde{\boldsymbol{s}} = \boldsymbol{B}_f\tilde{f}. \tag{5.4}$$

Equation (5.4) is subjected to two inlet and two outlet boundary conditions. The solution forced only in u at the nozzle satisfies $\tilde{h} = 0$ and $\tilde{u} = 1$, while for the one that is forced in both h and u, $\tilde{h}$ and $\tilde{u}$ can be chosen arbitrarily. We use the former when comparing the results with the nonlinear simulations (where the forcing was applied using the form (3.2)) whereas the latter when comparing to the spatial and WKBJ analysis of §§ 4.3 and 4.4.

Based on the results of the local and global analysis at $We_{in} = 1.75$, the convective instability of the flow ensures that, at the outlet, any existing k^+ branch, obtained from the spatial analysis, will be transmitted downstream. Since the relevant $k^+(\omega, L)$ branch for a given ω and at $z = L$ can be obtained from the local analysis of § 4.3, we impose for the solution of (5.4) at $z = L$ the spatial response, specifically, $\tilde{h}(L) = \hat{h}\exp(\mathrm{i}kL)$ and $\tilde{u}(L) = \hat{u}\exp(\mathrm{i}kL)$, k being the unique root of the dispersion relation corresponding to a downstream amplified wavenumber. It should be noted that, for active systems, such as the jet falling under the influence of gravity, it is not possible *a priori* to impose unique boundary conditions at the outlet. Thus, substitution of the resolvent response by the spatial response at the outlet should be treated as an approach to close the differential problem of (5.4) rather than depicting the physical boundary conditions. To ensure that these boundary conditions do not affect the final response over a given domain size L, we impose them for a domain size $L' > L$, such that the response for all the frequencies over L is independent of the imposed boundary condition.

Finally, we express the magnitude of the response $\tilde{\boldsymbol{s}}$ due to the externally applied forcing in terms of the gain G, with the maximum gain expressed as

$$G^2_{max}(L) = \max_{\omega} \frac{\|\tilde{\boldsymbol{s}}\|^2}{\|\tilde{\boldsymbol{f}}\|^2} = \max_{\omega} \frac{\|(\boldsymbol{M} + \mathrm{i}\omega \boldsymbol{I})^{-1} \boldsymbol{B}_f \tilde{\boldsymbol{f}}\|^2}{\|\tilde{\boldsymbol{f}}\|^2}, \tag{5.5}$$

attained at ω_{opt}. To measure the amplitude of the response and the forcing, we define $\boldsymbol{Q}$ and $\boldsymbol{Q}_f$ as the weight matrices of the discretised energy norm ($\|\tilde{\boldsymbol{s}}\|^2 = \boldsymbol{s}^\dagger \boldsymbol{Q} \boldsymbol{s}$) and the forcing norm ($\|\tilde{\boldsymbol{f}}\|^2 = f^\dagger \boldsymbol{Q}_f f$), respectively, obtained for the Chebyshev space on the physical domain L that is mapped into the interval $-1 \leqslant y \leqslant 1$ by using the transformation $z = [(L/2) \times (y + 1)]$. Here $\boldsymbol{Q}_f$ is a $2N \times 2N$ matrix enabling us to distinguish forcing on u only or on both components u and h. Following the optimisation method using singular value decomposition (SVD) described in Marquet & Sipp (2010) and Garnaud *et al.* (2013), we then express the optimal gain using the following eigenvalue problem:

$$\boldsymbol{Q}_f^{-1} \boldsymbol{B}_f^\dagger (\boldsymbol{M} + \mathrm{i}\omega \boldsymbol{I})^{-1\dagger} \boldsymbol{Q}^\dagger (\boldsymbol{M} + \mathrm{i}\omega \boldsymbol{I})^{-1} \boldsymbol{B}_f \tilde{\boldsymbol{f}} = \lambda \tilde{\boldsymbol{f}}, \tag{5.6}$$

whose leading eigenvalue solution λ gives G^2_{max} and the associated eigenmode solution $\tilde{f}$ yields the optimal normalised forcing amplitude in (h, u) to be applied at the inlet.

Since the linear analysis is based on small perturbations, the exact amplitude of the perturbation is unaccounted for in expression (5.5). For the resolvent analysis we then define $G_{h,fu}$ as the gain in h from a solution forced only in u and $G_{q,fq}$ as the gain in $\boldsymbol{q}$ for a solution forced in $\boldsymbol{q}$, where $\boldsymbol{q} = [a, u]$. The two expressions for the gain, $G_{h,fu}$ and $G_{q,fq}$, are formulated to replicate the forcing and gain definitions in the nonlinear simulations (§ 3) and the spatial analysis (§ 4.3 and § 4.4), respectively.

Looking for the gain in $G_{q,fq}$ requires the inclusion of additional operators $\boldsymbol{P}$ and $\boldsymbol{H}$, which express $\boldsymbol{q}$ in terms of $\boldsymbol{s}$, and are given by

$$\tilde{\boldsymbol{q}} = \boldsymbol{P} \tilde{\boldsymbol{s}}, \tag{5.7a}$$

$$\tilde{f}_q = \boldsymbol{H} \tilde{\boldsymbol{f}}. \tag{5.7b}$$

The operator $\boldsymbol{H}$ modifies the imposed boundary conditions in terms of $\tilde{a}$, whereas the operator $\boldsymbol{P}$ adequately expresses the response in $\tilde{a}$ in terms of $\tilde{h}$ such that $\tilde{a} = 2h_b \tilde{h}$. Additionally, to have an explicit comparison with the spatial analysis, we apply a forcing at the inlet which is obtained as the eigenmode solution of the spatial problem in § 4.3. Thus,

$$\tilde{f}_q = \hat{\boldsymbol{q}}(z = 0). \tag{5.8}$$

The gain for the imposed forcing is then obtained as

$$G^2_{q,fq}(\omega) = \frac{\|\tilde{\boldsymbol{q}}\|^2}{\|\tilde{f}_q\|^2} = \frac{\|\boldsymbol{P}(\boldsymbol{M} + \mathrm{i}\omega \boldsymbol{I})^{-1} \boldsymbol{B}_f \boldsymbol{H}^{-1} \tilde{f}_q\|^2}{\|\tilde{f}_q\|^2}. \tag{5.9}$$

Note, however, that even though this formalism allows a direct comparison with the spatial analysis, the gain $G_{q,fq}(\omega)$ does not represent the maximum optimal gain since we do not impose the optimisation of the inlet forcing vector using an SVD formalism as was done in (5.6). Figure 11 demonstrates the difference between the gain and ω_{opt} computed using the direct mode from spatial analysis (in black) and through an optimisation problem that solves for the optimal mode (in blue). Indeed, the resolvent gain based on the optimised mode is much larger in magnitude.

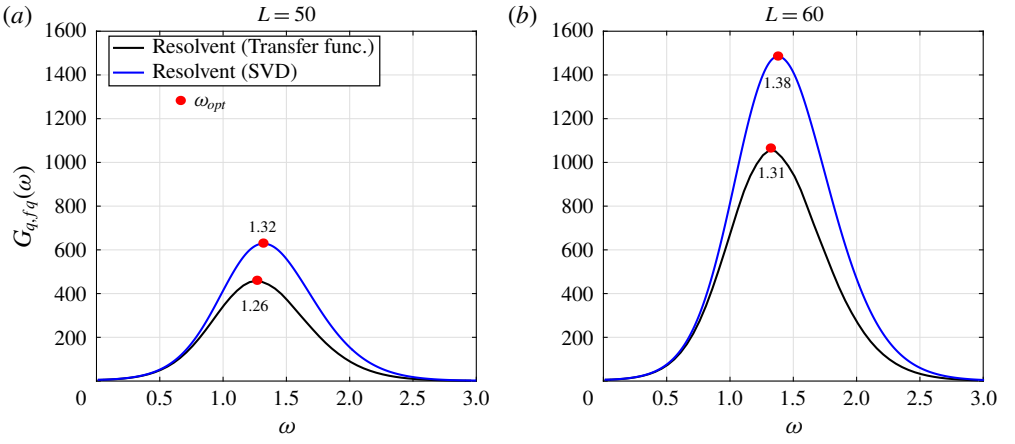

FIGURE 11. Comparison of the total gain at different frequencies from the resolvent analysis for domain sizes (*a*) $L = 50$ and (*b*) $L = 60$ and for the jet defined by $Oh_{in} = 0.3$, $Bo_{in} = 0.1$ and $We_{in} = 1.75$. The gain computed by applying the transfer function on the direct eigenmode from the spatial analysis is shown in black and the maximal optimal gain computed through the SVD analysis is shown in blue.

5.2.2. *Results: comparison with spatial stability analysis*

To replicate the type of forcing and the expression of gain used in the spatial analysis in §§ 4.3 and 4.4, we impose the eigenmode solution at the nozzle exit obtained from the spatial analysis as the forcing vector in the resolvent analysis. The resulting gains $G_{q,fq}$ for two different fixed domain sizes $L = 50$ and $L = 60$ are shown in figure 8. We observe from that figure that the inclusion of the amplitude equation in evaluating the spatial response by far improves the estimation of the true gain obtained from the resolvent analysis. Moreover, the predicted ω_{opt} producing the largest $G_{q,fq}$ from the WKBJ analysis is in close agreement with that of the resolvent analysis. The response norm obtained using the different approaches agrees qualitatively (see figure 22 later). Its non-monotonic behaviour at $\omega = 1.5$ (see figure 22*c–d*) is well captured and is in accordance with the work presented in Consoli-Lizzi (2016). However, the difference in gain between the three methods originates as a result of the quantitative disparity in the response obtained at different frequencies. The divergence between the spatial and resolvent analysis is due to the stretching effect of gravity on the base flow. For a parallel base flow, the results obtained from both methods are found to be identical (as shown in § A.4, figure 21).

5.2.3. *Results: comparison with nonlinear simulations*

We compare the resolvent analysis with the nonlinear simulations of § 3.3. Classically, the optimal forcing frequency ω_{opt} resulting in the maximum gain can be deduced by plotting the gain $G_{h,fu}$ as a function of ω for a fixed domain size L. For capillary jets, however, the domain size over which the perturbation grows cannot be fixed *a priori*. It is merely an outcome of the analysis, which should compare well with the value of l_c measured in the nonlinear simulations.

In order to circumvent this lack of consistency and in the absence of the knowledge of l_c, we first plot $G_{h,fu}$ as a function of increasing domain sizes L and for fixed ω as shown in figure 12(*a*), where the gain $G_{h,fu}(\omega, L)$ is computed for $\omega = [1\text{–}2.5]$ with

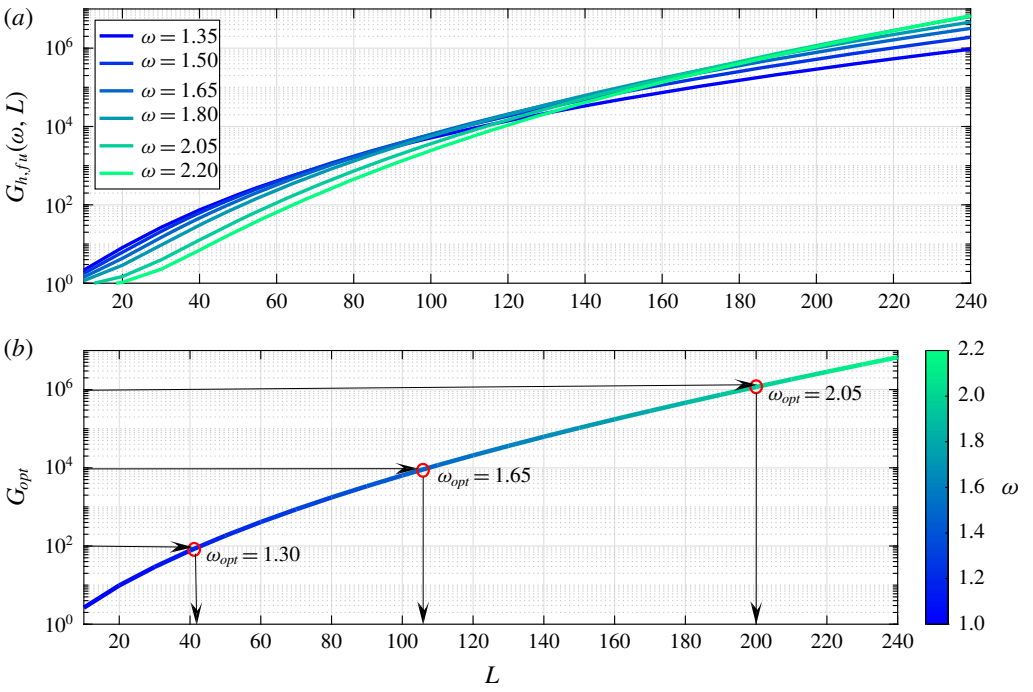

FIGURE 12. (*a*) Resolvent gain computed for $\tilde{h}$ with a forcing applied only in u for different values of domain sizes for a jet defined by $Oh_{in} = 0.3$, $Bo_{in} = 0.1$ and $We_{in} = 1.75$. Each curve is representative of a constant frequency. (*b*) The dominant frequency envelope as a function of the domain size L. The gain represented by 10^2, 10^4 and 10^6 is related to forcing amplitudes $\epsilon = 10^{-2}$, 10^{-4} and 10^{-6}, respectively. A horizontal projection from the respective gain on the frequency envelope yields ω_{opt}, and a vertical projection from the ω_{opt} on L determines the breakup length l_c.

$\Delta\omega = 0.01$ and for $L = [10\text{–}240]$ with $\Delta L = 10$. This results in a bundle of constant-frequency curves, intersecting each other at different locations in L. In figure 12(*a*) we now define the dominant frequency at a given L as the frequency with the maximum gain at L. A close examination reveals that there is a continuous transition in the dominant frequency as one moves along increasing domain sizes. This is shown in figure 12(*b*) where for clarity we plot only the envelope $G_{opt}(L)$ of the dominant frequency for all values of L. Thus $G_{opt}(L)$ is attained for $\omega_{opt}(L)$.

As discussed previously, L represents the breakup location along the jet where the nonlinear effects appear. Broadly speaking, nonlinearity enters the system when a small perturbation ϵ gives rise to a response of the order of 1, which suggests approximating l_c by the value of L at which

$$G_{opt}(l_c) \approx \frac{1}{\epsilon}. \tag{5.10}$$

In other words, the gain at the breakup location $L = l_c$ should be equal to $1/\epsilon$.

Using (5.10), we locate the gain in figure 12(*b*) for different forcing amplitudes $\epsilon = [10^{-2}\text{–}10^{-6}]$. At the given value of $G_{h,fu}$, a horizontal projection on the dominant frequency envelope will then decide the optimal forcing frequency for the given ϵ.

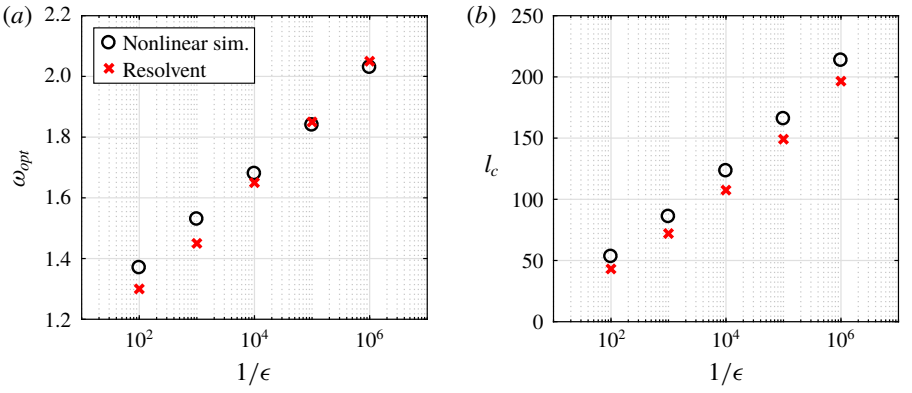

FIGURE 13. Comparison of breakup characteristics obtained from the nonlinear simulations (figure 3) and the resolvent analysis (figure 12) for a jet defined by $Oh_{in} = 0.3$, $Bo_{in} = 0.1$ and $We_{in} = 1.75$ for (*a*) the optimal forcing frequency ω_{opt} and (*b*) the breakup length l_c at different inverse forcing amplitudes $1/\epsilon$.

Finally, a vertical projection on L from the intersection point on the dominant frequency envelope will provide the relevant breakup length l_c for the forcing amplitude ϵ. Extracting the results from figure 12(*b*), we compare the optimal forcing frequency and the breakup length for different ϵ with the nonlinear solutions of § 3.3 in figure 13. The close quantitative agreement between the two approaches shows the strength of the resolvent analysis in predicting the ω_{opt} and l_c especially without any prior information from the nonlinear simulations. In figure 13 the small difference in values in the two methods can probably be attributed to *ad hoc* definition of the required threshold for nonlinear effects to kick in and breakup to occur. Finally, we would like to remind the reader that the dependence of ω_{opt} and l_c on the forcing amplitude ϵ, from the linear and nonlinear analysis presented above, qualitatively agrees with the linear results reported in Consoli-Lizzi (2016).

Note here that the jet breakup is a local phenomenon and conventionally the norm of the signal at L is used to define the breakup. However, in a global analysis, the pointwise norm of the field is not a definite norm. Using the infinity norm to define the breakup would have been an option, but is really not well suited to optimal growth calculations (see Foures, Caulfield & Schmid (2013) for a discussion). Hence, in our resolvent, spatial and WKBJ analysis, we always use an integral norm, the 2-norm, for the definition of the spatial gain.

6. Response to white noise

Up to now, we have only been interested in the response of the jet to an external disturbance characterised by a constant forcing frequency. However, in reality, the external disturbance is more likely to be composed of a broadband frequency rather than being harmonic. Thus, to model this physical perturbation, we carry out nonlinear simulations consistent with the scheme presented in § 3 by exciting the jet at the nozzle by white noise $\xi(t)$ defined in the time interval $[0,\ T]$ and formulated in a similar way as in Mantič-Lugo & Gallaire (2016). The white noise signal $\xi(t)$ is characterised by a constant power spectral density (PSD) $S_{\xi\xi}(\omega) = |\hat{\xi}(\omega)|^2$, where $\hat{\xi}(\omega)$

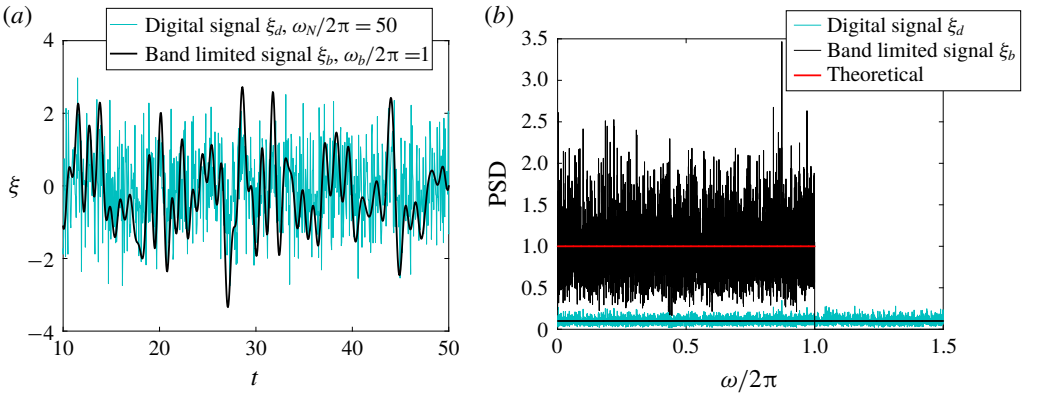

FIGURE 14. (*a*) White noise signal with unit power, comparing a signal without filter and filtered using a band limiting frequency $\omega_b/2\pi$. (*b*) PSD comparison of these two signals with their theoretical value. The PSD is estimated using a Welch method in MATLAB.

is the Fourier transform of $\xi(t)$ and has an infinite power P defined as

$$P = \frac{1}{T}\int_0^T |\xi_T(t)|^2\,\mathrm{d}t = \frac{1}{\pi}\int_0^\infty |\hat{\xi}|^2\,\mathrm{d}\omega = \sigma^2, \tag{6.1}$$

where σ is the variance. Even though pure white noise has infinite power (as $S_{\xi\xi}(\omega) > 0$), physical systems are usually characterised by a band-limited white noise. We thus filter the digital random signal $\xi_d(t)$ with a band limiting frequency $\omega_b/2\pi = 1$ to obtain the band-limited white noise $\xi_b(t)$ as shown in figure 14. For $\xi_d(t)$, the Nyquist frequency is set by $\omega_N/2\pi$, which depends on the time step (δt) of the signal, such that $\omega_N/2\pi = 1/2\delta t$. Here we chose $\delta t = 0.01$. The noise $\xi_b(t)$ is normalised to have zero mean, unit variance and unit power, with a constant value for the PSD, where $2|\hat{\xi}_b|^2 = 2\pi/\omega_b$, which completely depends on the band limiting frequency. Finally, we impose this filtered white noise as an inlet velocity condition for the jet defined by $Oh_{in} = 0.3$, $Bo_{in} = 0.1$ and $We_{in} = 1.75$ and governed by the equations (3.1) by replacing the boundary condition (3.2) with

$$\left.\frac{\mathrm{d}u}{\mathrm{d}t}\right|_{(0,t)} = \epsilon\xi_b(t), \tag{6.2}$$

where ϵ is the amplitude of the white noise signal. The forcing is applied at two different amplitudes, $\epsilon = 10^{-2}$ and 10^{-4}, and for large times ($T = 2000$) so as to achieve results that are time-independent. For the MATLAB solver `ode23tb` with varying step size, the maximum time step size is set as δt and white noise for intermediate time steps is obtained through interpolation.

At every pinch-off on the jet, we note the breakup length l_c, the pinch-off period ΔT_{po} and the drop radius R_{drop} at the time of breakup. The distribution of the breakup characteristics is shown as a histogram in figures 15 and 16 and compared with the expected response of the jet in the presence of the pure $\omega_{opt}(\epsilon)$, which corresponds to $\omega_{opt} = 1.38$ and 1.65 for $\epsilon = 10^{-2}$ and 10^{-4}, respectively. The breakup characteristics for ω_{opt} have been discussed in figure 2 and are depicted by red bars in figures 15 and 16.

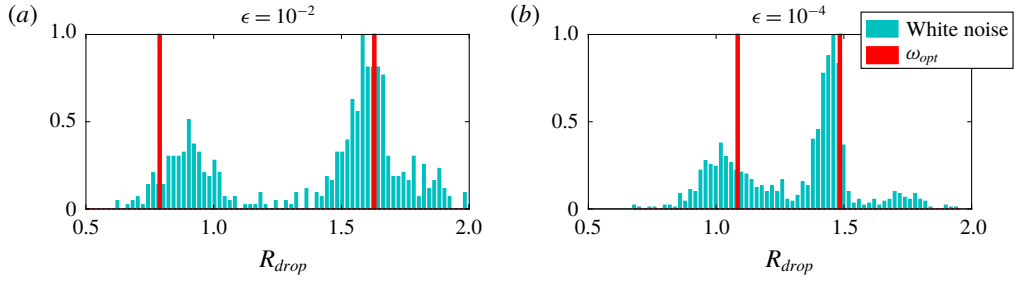

FIGURE 15. Comparison of the normalised frequency of the drop radius R_{drop} for a jet defined by $Oh_{in} = 0.3$, $Bo_{in} = 0.1$ and $We_{in} = 1.75$ and being forced at amplitude (*a*) $\epsilon = 10^{-2}$ and (*b*) $\epsilon = 10^{-4}$ by their respective optimal forcing frequency ω_{opt} (in red bars) and white noise (in cyan bars). For both the amplitudes, the white noise data are concentrated around two main drop sizes, representatives of the main and satellite drops. The most frequent drop sizes are $R_{drop} = 1.65$ and 1.45 for $\epsilon = 10^{-2}$ and 10^{-4}, respectively. These values are close to the ones predicted by the nonlinear simulations of figure 2, where the main drop size was predicted to be 1.62 and 1.48 for $\epsilon = 10^{-2}$ and 10^{-4}, respectively.

The drop size distribution shown in figure 15(*a*) highlights the two distribution peaks concentrated around $\approx$0.9 and $\approx$1.65, representing the group of satellite and main drops, respectively. This behaviour also exists for smaller $\epsilon = 10^{-4}$, where the radius is aggregated at $\approx$1.05 and $\approx$1.45. The results for the main drop size are coherent with the ones obtained in the presence of pure optimal forcing, where $R_{drop} = 1.62$ and 1.45 for $\epsilon = 10^{-2}$ and 10^{-4}, respectively. Thus, even in the presence of white noise, the response of the jet is dominated by its expected behaviour at ω_{opt}.

Unlike the drop radius, the peak of the distribution of breakup length obtained by imposing the white noise is not in close agreement with that of the optimal forcing as shown in figure 16(*a*,*b*). Yet, we clearly see that the distribution spectrum shifts to large values of breakup length as ϵ is decreased, a behaviour similar to the one predicted by ω_{opt}, where l_c increases from $\approx$50 to $\approx$125 as ϵ is decreased. The distribution spectrum shifts due to the presence of forcing frequencies other than the optimal one, owing to which the breakup length is known to show a large variation, as is evident from figure 1. In the absence of white noise, a similar rationale should not be applied when evaluating the effect of a given pair of forcing frequencies. Indeed, their collective effect on the breakup characteristics could be different from their individual responses, as was demonstrated in the case of parallel jets (Driessen *et al.* 2014).

Similar conclusions can be drawn for the comparison of ΔT_{po} between white noise forcing and forcing with ω_{opt} from figure 16(*c*,*d*) where we plot the breakup period between two consecutive drops.

7. Conclusion and perspectives

In this work, we inspect the response of a spatially varying gravitationally stretched jet subjected to an inlet velocity perturbation. The forcing is characterised through the frequency and the amplitude, the latter playing a major role in the determination of the optimal forcing frequency. The results of the numerical simulations performed on the nonlinear 1-D Eggers & Dupont (1994) equations show an increase in optimal forcing frequency and the breakup length as the forcing amplitude is decreased.

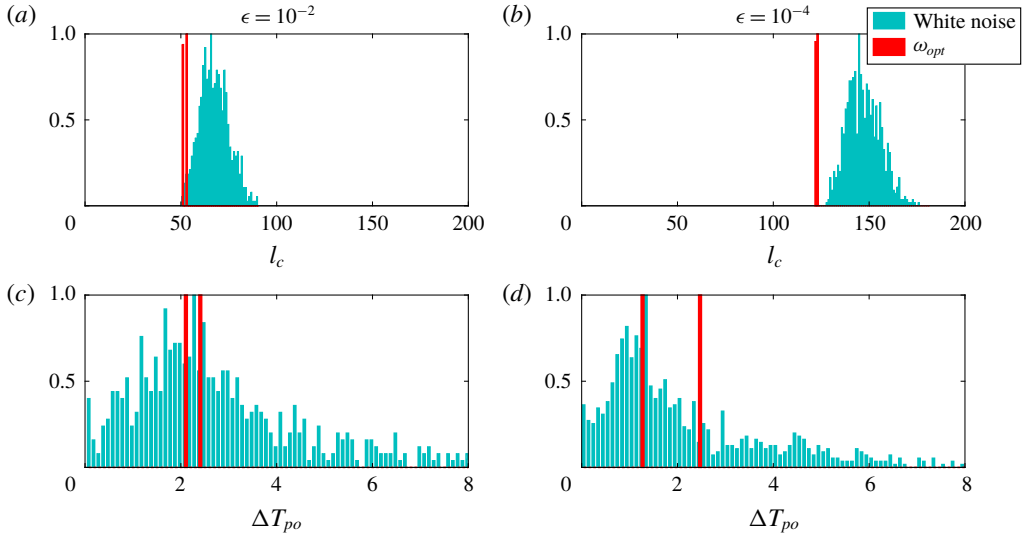

FIGURE 16. (*a*,*b*) Comparison of the normalised frequency of the breakup length l_c and (*c*,*d*) comparison of the normalised frequency of the breakup period ΔT_{po}, each for a jet defined by $Oh_{in} = 0.3$, $Bo_{in} = 0.1$ and $We_{in} = 1.75$: (*a*,*c*) are subjected to a forcing amplitude $\epsilon = 10^{-2}$ and (*b*,*d*) to $\epsilon = 10^{-4}$. The data in red correspond to the optimal forcing frequency ω_{opt} and data in cyan to white noise. The most frequent white noise breakup length is close to the l_c prediction in the presence of the ω_{opt}. For $\epsilon = 10^{-2}$ and 10^{-4}, the peak breakup period $\Delta T_{po} = 2.45$ and 1.35, respectively, and is in close proximity to the results obtained from the nonlinear simulations of figure 2.

We found that the amplitude-dependent preferred mode is a characteristic of gravity-driven jets only. A pure capillary jet, the base state of which is independent of gravity-induced stretching, does not sustain such behaviour. In such cases, decreasing the forcing amplitude only resulted in an increase of the breakup length, with the optimal frequency remaining fixed at all amplitudes.

The linear stability theory characterised the jet flow used for nonlinear simulations as locally unstable and globally stable. Based on the absolute–convective transition criteria, we analysed the local stability at each section along the axial direction. The solution of the dispersion relation and the subsequent analysis for the downstream-propagating spatial waves helped in confirming the predominant wave to be used for the zeroth-order spatial gain expression. The strong non-parallelism of the base flow close to the nozzle motivated the incorporation of the WKBJ framework, which markedly improved the prediction of the optimal forcing frequency in comparison to the resolvent analysis. However, the spatial gain was still observed to be lower than the resolvent. As suggested by Le Dizès & Villermaux (2017), using advanced stability tools (Schmid 2007), which accounts for non-parallel effects and non-modal growth, leads to an estimation of a more realistic spatial response.

This task was tackled using a resolvent analysis, which accurately captured the linear response of stable jets in the presence of an external forcing. Assuming a simple global amplitude breakup threshold criterion, the linear resolvent analysis becomes capable of predicting both the breakup length and the optimal forcing frequency given the amplitude of the forcing. The results of the nonlinear simulations and the resolvent for different forcing amplitudes are quantitatively comparable, thus

underlining the importance of the resolvent analysis. Additionally, the results have a qualitative agreement with the linear response analysis presented in Consoli-Lizzi (2016). Besides forcing the jet inlet with a fixed frequency, we also studied the response to white noise, to analyse its natural response to a distributed forcing frequency range. Surprisingly, even in the presence of white noise, the dominant response of the jet is close to that seen from the optimal frequency at that amplitude. These simulations also indicate the plausible reasons behind the large deviation observed for the frequency and breakup length in the unforced jet experiments of Consoli-Lizzi (2016).

In the presence of external forcing, a dominant feature seen from the nonlinear simulations is the formation of a main and a satellite drop at the time of breakup. Nevertheless, to properly examine the consequence of the forcing amplitude on the final drop size, there is a need to enhance the nonlinear model by including the physics of drop coalescence and disintegration, as done by Driessen & Jeurissen (2011). Post breakup, the state of the jet after the pinch-off should be inferred from the system before the breakup. Additionally, the choice for drop curvature is of paramount importance since a given breakup can possess a variety of drop shapes – each on a different length scale (Kowalewski 1996).

On a different note, if the final aim is to eliminate the presence of satellite drops, the forcing should be modified such that it leads to the selective production of equi-sized drops. In this direction the work of Chaudhary & Redekopp (1980), who controlled satellite drops by forcing the jet with a suitable harmonic added to the fundamental, and Driessen *et al.* (2014), who controlled the size of the droplet breaking off from a parallel jet by imposing a superposition of two Rayleigh–Plateau-unstable modes on the jet, could serve as the basis for formulating a theory for spatially varying gravity jets.

Acknowledgements

I.S. thanks the Swiss National Science Foundation (grant no. 200021-159957). The authors would like to thank E. Yim for extremely valuable discussions on the modelling of white noise disturbance and in the interpretation of the local/global response. The authors would also like to thank T. Ansaldi and G. Rocca, who worked on the foundation of the numerical code for parallel jets, as well as A. J. P. Bressy for efficiently performing several simulations on the enhanced version of the numerical code provided to him.

Declaration of interests

The authors report no conflict of interest.

Appendix A

A.1. *Numerical base-state solution validation*

In this appendix, we show the validation of our numerically obtained base-state solution of the governing equation (2.5) with the experimental results of Rubio-Rubio *et al.* (2013) for three different jet flows. The MATLAB `bvp4c` solver along with the boundary conditions stated in § 2 accurately capture the stretching (necking) close to the nozzle due to the effect of Bo_{in} as shown in figure 17.

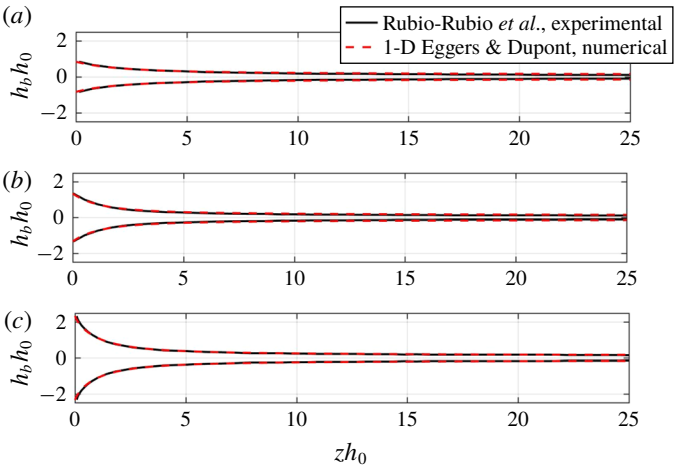

FIGURE 17. Comparison of the steady-state solution with results from Rubio-Rubio *et al.* (2013) for: (*a*) $Oh_{in} = 2.117$, $We_{in} = 2.62 \times 10^{-2}$, $Bo_{in} = 0.71$; (*b*) $Oh_{in} = 0.4799$, $We_{in} = 6.06 \times 10^{-3}$, $Bo_{in} = 1.81$; and (*c*) $Oh_{in} = 0.7238$, $We_{in} = 1.85 \times 10^{-3}$, $Bo_{in} = 5.53$.

A.2. *Effect of initial condition on breakup characteristics*

This section demonstrates the effect on breakup characteristics due to different initial conditions of the jet. Using the scheme described in § 3.2, we perform numerical solutions for a jet with $Oh_{in} = 0.3$, $We_{in} = 1.75$ and $Bo_{in} = 0.1$ excited with a forcing of amplitude $\epsilon = 10^{-2}$ and frequency $\omega = 0.8$. In the first case, the jet is initialised as a circular tip of radius 1 (figure 18*a*), and in the second case with the base-state solution obtained by solving (2.5) defined for an axial length of 100 (figure 18*b*). In both cases the numerical domain is considered large enough to capture all the breakups. As shown in figure 18, both the jets with different initial conditions have different transient dynamics up to $t = 55$ (tip) and $t = 40$ (base state) after which they enter the permanent regime. In this regime, the breakup length l_c and period ΔT_{po} are identical as shown in figure 18(*c*,*d*), respectively. It is thus safe to conclude that, in the permanent regime, the jet breakup is independent of the initial base-state solution.

A.3. *Numerical scheme validation*

In this appendix, we show the validation of our numerical scheme described in § 3.2 for the simulations of reduced 1-D Eggers & Dupont (1994) equations represented by equation (3.1). For the purpose of validation, we use the numerical data of van Hoeve *et al.* (2010), which are described for micro-jets of initial radius $h_0 = 18.5$ μm with density $\rho = 1098$ kg m^{-3}, viscosity $\eta = 3.65$ mPa s and surface tension $\gamma = 67.9$ mN m^{-1}. The jet is injected at a constant flow rate $Q = 0.35$ ml min^{-1}, corresponding to an initial jet velocity $U_0 = Q/(\pi h_0^2) = 5.4$ m s^{-1}. The flow can thus be described by the dimensionless numbers $Oh_{in} = 0.1$ and $We_{in} = 8.7$. Since the gravity effects are not considered in the experiment, we inject $Bo_{in} = 0$ in (3.1). To initiate jet breakup in their numerical simulations, a harmonic modulation of the dimensional nozzle radius is applied as follows:

$$h(z = 0, t) = h_0 + \delta \sin(2\pi n t), \tag{A 1}$$

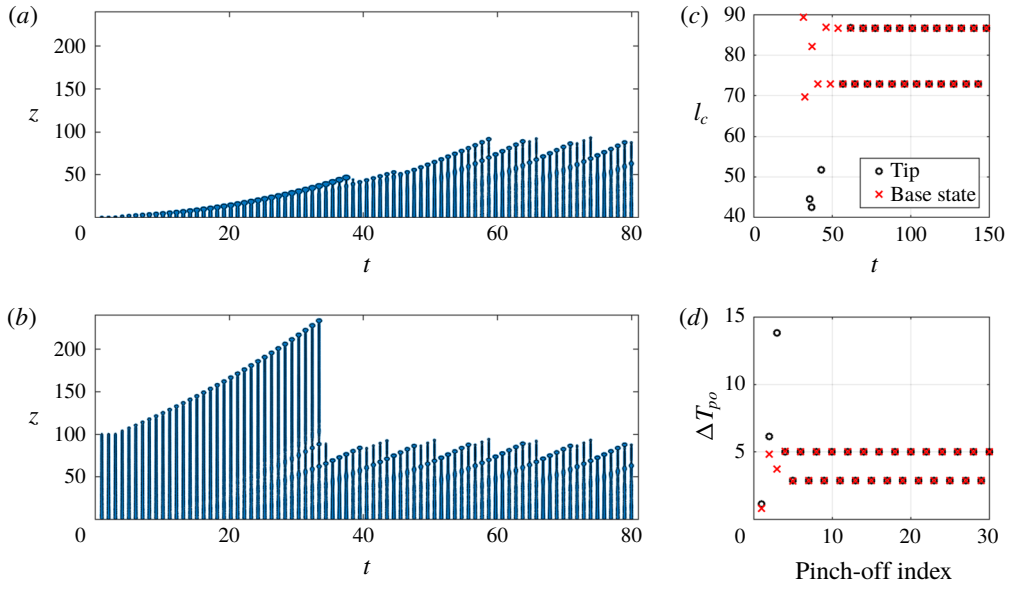

FIGURE 18. Time-sequence plot of a simulation with $Oh_{in} = 0.3$, $We_{in} = 1.75$ and $Bo_{in} = 0.1$ excited with a forcing of amplitude $\epsilon = 10^{-2}$ and frequency $\omega = 0.8$ and initialised (*a*) as a tip and (*b*) using the base-state solution. Comparisons of the breakup length and period for the two cases are presented in (*c*) and (*d*), respectively.

with $\delta/h_0 \approx 0.005$ the forcing amplitude and n the driving frequency. The latter is selected to match the optimum wavelength λ_{opt} for jet breakup, that is, $n = U_0/\lambda_{opt}$. To ensure a constant flow rate Q through the nozzle, the dimensional velocity is modulated correspondingly as

$$u_0(z = 0, t) = \frac{h_0^2 U_0}{[h(z = 0, t)]^2}. \tag{A 2}$$

The amplitude of the wave imparted by the forcing at the nozzle grows until it equals the radius of the jet. Pinch-off or jet breakup is then defined as when the minimum width of the jet is below a predefined value set to $10^{-3}h_0$.

In our numerical simulations, we compute solutions to the governing equation (3.1) with the same harmonic forcing and flow parameters as in van Hoeve *et al.* (2010). A hemispherical droplet described by $h = ({h_0}^2 - z^2)^{1/2}$ is used as initial condition for the shape of the jet, the tip of which is therefore initially at $z = h_0$. The velocity is initialised to u_0 everywhere along the jet. A fixed number of grid points, corresponding to a discretisation size $\mathrm{d}z = 0.05$, is uniformly distributed throughout the entire domain. The final validation is presented in figure 19, which shows a comparison of the time series of the dynamics of jet breakup obtained from our numerical scheme and the numerical results from van Hoeve *et al.* (2010).

For both parts of figure 19, the evolution of the jet shape is shown at time intervals of 2 μs. Our numerical model predicts a breakup period of 25 μs and a breakup length of 856 μm. The results of van Hoeve *et al.* (2010) have a breakup period of approximately 26 to 30 μs and a breakup length of approximately 800 μm. The error in breakup length between the two codes can be explained by the difference in

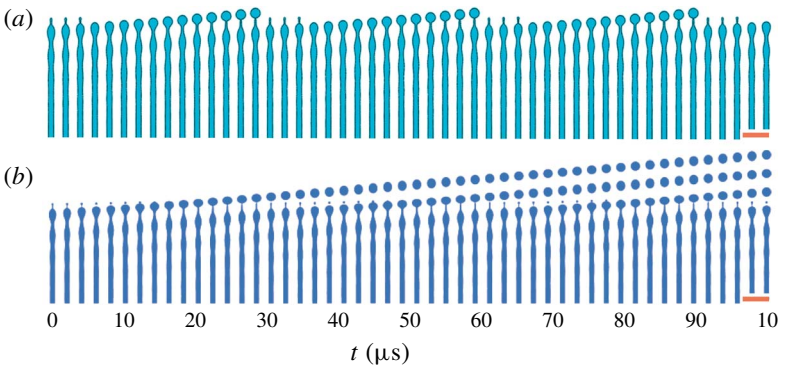

FIGURE 19. Numerical solutions of the governing equation (3.1) for a jet in an inert medium with $Oh_{in} = 0.1$, $We_{in} = 8.7$ and $Bo_{in} = 0$. (*a*) Results from our numerical scheme described in § 3.2 and (*b*) experimentally validated numerical results of van Hoeve *et al.* (2010). The red bar corresponds to a length scale of 200 μm.

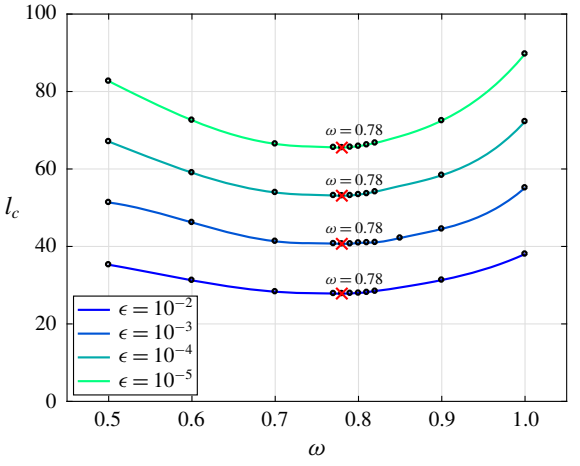

FIGURE 20. Nonlinear simulation results for optimal forcing frequency ω_{opt} carried out for jet characteristics $Oh_{in} = 0.3$, $We_{in} = 1.75$ and $Bo_{in} = 0$. The breakup length l_c is plotted as a function of forcing frequency ω for different forcing amplitudes ϵ.

grid size. Overall, figure 19 shows a good agreement between the two sets of results and validates our numerical scheme.

A.4. *Comparison between resolvent and spatial analyses*

In this section, we briefly show the preferred forcing frequency of the jet discussed in § 3.3 in the absence of gravity. The jet is characterised by $Oh_{in} = 0.3$, $We_{in} = 1.75$ and $Bo_{in} = 0$. As shown in figure 20, nonlinear simulations for the governing equations (3.1) for the zero-gravity case using different forcing amplitudes ϵ show that ω_{opt} is independent of the chosen forcing amplitude, a behaviour in contrast to the situation where gravity is present (previously shown in figure 3). Figure 21 shows the comparison of gain, in the absence of gravity, as a function of forcing frequency using spatial and resolvent analysis for two different domain sizes. For convenience,

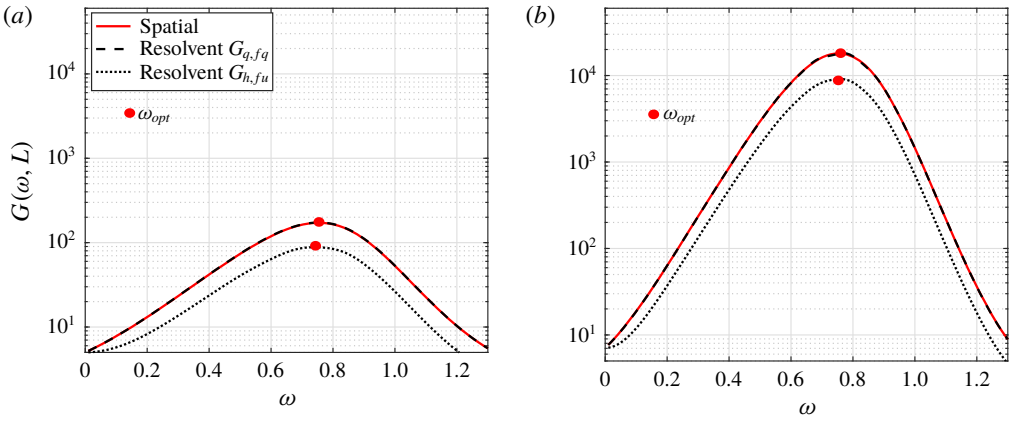

FIGURE 21. Comparison of gain and ω_{opt} obtained from the resolvent analysis and spatial analysis for two different domain sizes (*a*) $L = 25$ and (*b*) $L = 50$ for a jet in the absence of gravity and characterised by $Oh = 0.3$ and $We = 1.75$. Irrespective of the domain size and the method employed, the ω_{opt} value lies in the range [0.74, 0.75].

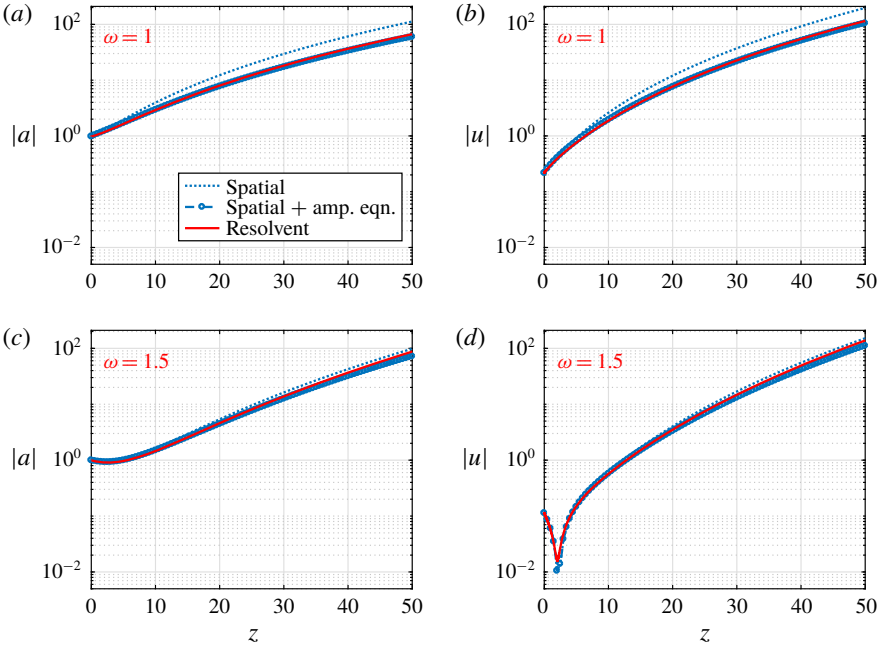

FIGURE 22. Resolvent and spatial response ($|a|$ and $|u|$) of the jet characterised by $Oh_{in} = 0.3$, $We_{in} = 1.75$ and $Bo_{in} = 0.1$ at (*a*,*b*) $\omega = 1$ and (*c*,*d*) $\omega = 1.5$ with a domain size $L = 50$.

we also plot the resolvent gain $G_{h,fu}$ expressed in terms of the forcing applied for the nonlinear simulations. We note that all the curves, irrespective of the domain size, predict the same optimal forcing frequency $\omega_{opt} = 0.74$–0.76, a value close to the nonlinear prediction of figure 20. Moreover, unlike the situation with $Bo = 0.1$, we

notice that, in the absence of gravity, the magnitude of the gain at all frequencies is well captured by the spatial analysis.

A.5. *Linear operator for eigenvalue problem*

For the eigenvalue problem related to the global stability in § 5.1, the matrix $\boldsymbol{M}$ is expressed as

$$\boldsymbol{M} = \begin{bmatrix} M_{11} & M_{12} \\ M_{21} & M_{22} \end{bmatrix}, \tag{A 3}$$

where the expressions M_{11}, M_{12}, M_{21} and M_{22} denote the following differential equations:

$$M_{11} = -\frac{\boldsymbol{Q}}{h_b^2}\mathrm{D} + \frac{\boldsymbol{Q}h_b'}{h_b^3}\boldsymbol{I}, \tag{A 4a}$$

$$M_{12} = -\frac{h_b}{2}\mathrm{D} - h_b'\boldsymbol{I}, \tag{A 4b}$$

$$M_{21} = \sum_{k=1}^{4} s^{2k-1}\boldsymbol{T}_k - 12Oh_{in}\boldsymbol{Q}\left(\frac{h_b'^2}{h_b^2} + \frac{h_b''}{h_b}\right)\mathrm{D}, \tag{A 4c}$$

$$M_{22} = 3Oh_{in}\left(\mathrm{D}^2 + \frac{2h_b'}{h_b\mathrm{D}}\right) - \frac{\boldsymbol{Q}}{h_b^2}\mathrm{D} + \frac{2\boldsymbol{Q}h_b'}{h_b^3}\boldsymbol{I}. \tag{A 4d}$$

In the group of equations (A 4), $\boldsymbol{I}$ is the identity operator, $\mathrm{D}^n \equiv \mathrm{d}^n/\mathrm{d}z^n$, $s(z) = [1 + (h_b')^2]^{-1/2}$ and

$$T_1 = \frac{1}{r_b^2}\mathrm{D} - \frac{2r_b'}{r_b^3}\boldsymbol{I}, \tag{A 5a}$$

$$T_2 = \mathrm{D}^3 + \frac{h_b'}{h_b}\mathrm{D}^2 - \left[\frac{(h_b')^2}{h_b^2} + \frac{h_b''}{h_b}\right]\mathrm{D} - \frac{rh_b'h_b''}{h_b^2}\boldsymbol{I}, \tag{A 5b}$$

$$T_3 = -6h_b'h_b''\mathrm{D}^2 - 3\left[\frac{(h_b')^2h_b''}{h_b} + (h_b'')^2 - h_b'h_b'''\right]\mathrm{D}, \tag{A 5c}$$

$$T_4 = 15(h_b'')^2(h_b')^2\mathrm{D}. \tag{A 5d}$$

A.6. *WKBJ formulation for axisymmetric 1-D Eggers and Dupont equations*

A.6.1. *Linearised equations*

Considering linear perturbations (a', u') in the jet interface and velocity around the base flow (a_b, u_b), the linearised system of equations is written as

$$\frac{\partial a'}{\partial t} = (-A_1 - A_2\mathrm{D}_1)a' + (-A_3 - A_4\mathrm{D}_1)u', \tag{A 6a}$$

$$\frac{\partial u'}{\partial t} = (-B_1 - B_2\mathrm{D}_1 - B_3\mathrm{D}_2 - B_4\mathrm{D}_3)a' + (-B_1 - B_2\mathrm{D}_1 - B_3\mathrm{D}_2)u', \tag{A 6b}$$

where D_i with $i = 1, \ldots, 3$ are the differential operators with respect to z. Equation (A 5) can be reformed as

$$[\dot{\boldsymbol{q}}'] = \boldsymbol{K}[\boldsymbol{q}'], \tag{A 7}$$

where

$$[\boldsymbol{q}'] = \begin{bmatrix} a' \\ u' \end{bmatrix}, \quad \boldsymbol{K} = \begin{bmatrix} -A_1 - A_2\mathrm{D}_1 & -A_3 - A_4\mathrm{D}_1 \\ -B_1 - B_2\mathrm{D}_1 - B_3\mathrm{D}_2 - B_4\mathrm{D}_3 & -B_5 - B_6\mathrm{D}_1 - B_7\mathrm{D}_2 \end{bmatrix}, \quad (\mathrm{A}\,8a,b)$$

where the coefficients $A_{1,\ldots,4}$ and $B_{1,\ldots,7}$ are given as

$$A_1 = {u_b}'(z), \quad (\mathrm{A}\,9a)$$
$$A_2 = u_b(z), \quad (\mathrm{A}\,9b)$$
$$A_3 = {a_b}'(z), \quad (\mathrm{A}\,9c)$$
$$A_4 = a_b(z), \quad (\mathrm{A}\,9d)$$

$$B_1 = \frac{15(-2{a_b}'(z)^3 - 4a_b(z){a_b}'(z) + {a_b}'(z)^3(-{a_b}''(z)) + a_b(z){a_b}'(z){a_b}''(z)^2)}{16S^{7/2}} - \frac{3(2a_b(z){a_b}^{(3)}(z) - 8{a_b}'(z) + {a_b}'(z){a_b}''(z)^2 - 2{a_b}'(z){a_b}''(z))}{8S^{5/2}} + \frac{{a_b}^{(3)}(z)}{2S^{3/2}} - \frac{3(Oh_{in}{a_b}'(z){u_b}'(z))}{a_b(z)^2}, \quad (\mathrm{A}\,9e)$$

$$B_2 = \frac{15(-2{a_b}'(z)^4 - 4a_b(z){a_b}'(z)^2 + {a_b}'(z)^4(-{a_b}''(z)) + a_b(z){a_b}'(z)^2{a_b}''(z)^2)}{32S^{7/2}} - \frac{3(a_b(z){a_b}''(z)^2 - 8{a_b}'(z)^2 + a_b(z){a_b}^{(3)}(z){a_b}'(z) - 4{a_b}'(z)^2{a_b}''(z) - 4a_b(z))}{8S^{5/2}} - \frac{(a_b''(z) + 2)}{2S^{3/2}} + \frac{3Ohu_b'(z)}{a_b(z)}, \quad (\mathrm{A}\,9f)$$

$$B_3 = \frac{3({a_b}'(z)^3 - 2a_b(z){a_b}'(z){a_b}''(z))}{8S^{5/2}} - -\frac{{a_b}'(z)}{2S^{3/2}}, \quad (\mathrm{A}\,9g)$$
$$B_4 = \frac{a_b(z)}{2S^{3/2}}, \quad (\mathrm{A}\,9h)$$
$$B_5 = -{u_b}'(z), \quad (\mathrm{A}\,9i)$$
$$B_6 = \frac{3Oh_{in}{a_b}'(z)}{a_b(z)} - u_b(z), \quad (\mathrm{A}\,9j)$$
$$B_7 = 3Oh. \quad (\mathrm{A}\,9k)$$

In the above equations S replaces the term $\frac{1}{4}{a_b}'(z)^2 + a_b(z)$.

A.6.2. *Linearised equation expressed in terms of slow variable*

For the WKBJ analysis, we then introduce the spatial scales. The fast spatial scale z is replaced by the slow scale Z, such that $Z = \eta z$. The base flow is now expressed as a function of Z such that $a_b(Z)$ and $u_b(Z)$. Let us consider the following normal-mode expansion for the perturbation:

$$\boldsymbol{q}'(Z, t) = \hat{\boldsymbol{q}}(Z) \exp\left[\mathrm{i}\left(\frac{1}{\eta}\int_0^Z k(Z', \omega)\,\mathrm{d}Z' - \omega t\right)\right]. \quad (\mathrm{A}\,10)$$

Injecting the transformations (A 11*a–d*) into (A 5), the linearised equations on a weakly non-parallel base flow are expressed through (A 12)–(A 13):

$$\left.\begin{aligned}
\frac{\partial}{\partial t} &\to -\mathrm{i}\omega,\\
\frac{\partial}{\partial z} &\to \mathrm{i}k + \eta\frac{\partial}{\partial Z},\\
\frac{\partial^2}{\partial z^2} &\to -k^2 + \mathrm{i}\eta\left(\frac{\partial k}{\partial Z} + 2k\frac{\partial}{\partial Z}\right) + \eta^2\frac{\partial^2}{\partial Z^2},\\
\frac{\partial^3}{\partial z^3} &\to -\mathrm{i}k^3 - 3\eta k\left(\frac{\partial k}{\partial Z} + k\frac{\partial}{\partial Z}\right)\\
&\quad + \eta^2\left(3\mathrm{i}\frac{\partial k}{\partial Z}\frac{\partial}{\partial Z} + 3\mathrm{i}k\frac{\partial^2}{\partial Z^2} + \mathrm{i}\frac{\partial^2 k}{\partial Z^2}\right) + \eta^3\frac{\partial^3}{\partial Z^3},
\end{aligned}\right\} \qquad (\mathrm{A}\,11a\text{–}d)$$

where the continuity equation converts to

$$(-\mathrm{i}\omega + \mathrm{i}ku_b)\hat{a} + (\mathrm{i}ka_b)\hat{u} = -\eta\left[\frac{\partial}{\partial Z}(a_b\hat{u} + u_b\hat{a})\right], \qquad (\mathrm{A}\,12)$$

and the momentum equation transforms as

$$\begin{aligned}
\mathrm{i}\omega\hat{u} \;=\; & -\eta\frac{\partial u_b}{\partial Z}\hat{u} - \left(u_b - \eta\frac{3Oh}{a_b}\frac{\partial a_b}{\partial Z}\right)\left(\eta\frac{\partial}{\partial Z} + \mathrm{i}k\right)\hat{u}\\
& + 3Oh\left(-k^2 + \eta\mathrm{i}\left(\frac{\partial k}{\partial Z} + 2k\frac{\partial}{\partial Z}\right) + \eta^2\frac{\partial^2}{\partial Z^2}\right)\hat{u} - \left(\eta\frac{3}{4a_b^{5/2}}\frac{\partial a_b}{\partial Z}\right)\hat{a}\\
& + \left(\frac{1}{2a_b^{3/2}} + \frac{3\eta Oh}{a_b}\frac{\partial u_b}{\partial Z}\right)\left(\eta\frac{\partial}{\partial Z} + \mathrm{i}k\right)\hat{a}\\
& - \frac{\eta}{2a_b^{3/2}}\frac{\partial a_b}{\partial Z}\left(-k^2 + \eta\mathrm{i}\left(\frac{\partial k}{\partial Z} + 2k\frac{\partial}{\partial Z}\right) + \eta^2\frac{\partial^2}{\partial Z^2}\right)\hat{a}\\
& + \frac{1}{2a_b^{1/2}}\left(-\mathrm{i}k^3 - 3\eta k\left(\frac{\partial k}{\partial Z} + k\frac{\partial}{\partial Z}\right) + O(\eta^2)\right)\hat{a}.
\end{aligned} \qquad (\mathrm{A}\,13)$$

Defining $\hat{\boldsymbol{q}}^{(1)} = [\hat{a}^{(1)}\ \ \hat{u}^{(1)}]$ and $\hat{\boldsymbol{q}}^{(2)} = [\hat{a}^{(2)}\ \ \hat{u}^{(2)}]$, we now consider the asymptotic expansion

$$\hat{\boldsymbol{q}} \sim A(Z)\hat{\boldsymbol{q}}^{(1)}(Z) + \eta\hat{\boldsymbol{q}}^{(2)}(Z) + \cdots, \qquad (\mathrm{A}\,14)$$

and inject it into the governing equations (A 12)–(A 13) to obtain the local stability problem at orders η^0 and η^1.

Order η^0. At zeroth order in η, the local stability problem is retrieved:

$$\underbrace{(-\mathrm{i}\omega + \mathrm{i}ku_b)}_{L_{11}}\hat{a}^{(1)} + \underbrace{(\mathrm{i}ka_b)}_{L_{12}}\hat{u}^{(1)} = 0, \qquad (\mathrm{A}\,15a)$$

$$\underbrace{-\frac{\mathrm{i}k}{2a_b^{3/2}}(1 - k^2a_b)}_{L_{21}}\hat{a}^{(1)} + \underbrace{(-\mathrm{i}\omega + \mathrm{i}ku_b + 3Ohk^2)}_{L_{22}}\hat{u}^{(1)} = 0. \qquad (\mathrm{A}\,15b)$$

The system of equations represented by (A 15) can be reframed using the linear operator $\boldsymbol{L}$, such that

$$\boldsymbol{L}[\hat{\boldsymbol{q}}^{(1)}] = 0, \quad \text{where the linear operator } \boldsymbol{L} = \begin{bmatrix} L_{11} & L_{12} \\ L_{21} & L_{22} \end{bmatrix}. \tag{A 16}$$

Substituting the expression for $\hat{u}^{(1)}$ from (A 15*a*) into (A 15*b*), we finally obtain

$$\left(-\omega^2 + 2u_b\omega k + \left(-\frac{1}{2\sqrt{a_b}} - u_b^2 - 3\mathrm{i}Oh\omega\right)k^2 + 3\mathrm{i}Ohu_bk^3 + \frac{\sqrt{a_b}}{2}k^4\right)\hat{a}^{(1)} = 0, \tag{A 17}$$

the solution of which gives the four roots of k for a given ω. The relevant k branch is tracked as discussed in § 4. For a given ω and a predetermined k, the solution of the linear problem (A 16) gives the response $\hat{\boldsymbol{q}}^{(1)}$, a parameter needed to solve the local stability problem at order η^1.

Order η^1. At first order we obtain

$$\boldsymbol{L}[\hat{\boldsymbol{q}}^{(2)}] = \boldsymbol{Q}[A\hat{\boldsymbol{q}}^{(1)}], \tag{A 18}$$

where the operator $\boldsymbol{Q}$ can be split into two parts:

$$\boldsymbol{Q}[A\hat{\boldsymbol{q}}^{(1)}] = \boldsymbol{R}[\hat{\boldsymbol{q}}^{(1)}]\frac{\mathrm{d}A}{\mathrm{d}Z} + \boldsymbol{S}[\hat{\boldsymbol{q}}^{(1)}]A. \tag{A 19}$$

Here the operator $\boldsymbol{R}$ is expressed as

$$\boldsymbol{R} = \begin{bmatrix} -u_b & -a_b \\ \left(\dfrac{1-3k^2a_b}{2a_b^{3/2}}\right) & (6\mathrm{i}Ohk - u_b) \end{bmatrix}, \tag{A 20}$$

and $\boldsymbol{S}$ is defined as

$$\boldsymbol{S} = \begin{pmatrix} s_{11} & s_{12} \\ s_{21} & s_{22} \end{pmatrix},$$

where the individual parameters are expressed as

$$s_{11} = -\frac{\partial u_b}{\partial Z} - u_b\frac{\partial}{\partial Z},$$
$$s_{12} = -\frac{\partial a_b}{\partial Z} - a_b\frac{\partial}{\partial Z},$$
$$s_{21} = \frac{3\mathrm{i}Ohk}{a_b}\frac{\partial u_b}{\partial Z} - \frac{1}{4a_b^{5/2}}\left((3-2k^2a_b)\frac{\partial a_b}{\partial Z} + 6ka_b^2\frac{\partial k}{\partial Z} + 2a_b(-1+3k^2a_b)\frac{\partial}{\partial Z}\right),$$
$$s_{22} = 3\mathrm{i}Oh\left(\frac{k}{a_b}\frac{\partial a_b}{\partial Z} + \frac{\partial k}{\partial Z} + 2k\frac{\partial}{\partial Z}\right) - u_b\frac{\partial}{\partial Z} - \frac{\partial u_b}{\partial Z}.$$

As explained in Huerre & Rossi (1998) and Viola *et al.* (2016), in order to have solutions of the inhomogeneous equation $\boldsymbol{L}[\hat{\boldsymbol{q}}^{(2)}] = \boldsymbol{Q}[A\hat{\boldsymbol{q}}^{(1)}]$, the forcing term $\boldsymbol{Q}$ should be in the image of the operator $\boldsymbol{L}$. This implies that $\boldsymbol{Q}$ should be orthogonal to the

corresponding adjoint eigenfunction $\tilde{\boldsymbol{q}}^{(1)}$ of the adjoint operator $\tilde{\boldsymbol{L}}$, with respect to the defined inner product,

$$\underbrace{R[\hat{\boldsymbol{q}}^{(1)}]\tilde{\boldsymbol{q}}^{(1)}\frac{\mathrm{d}A}{\mathrm{d}Z}}_{M(Z)}+\underbrace{S[\hat{\boldsymbol{q}}^{(1)}]\tilde{\boldsymbol{q}}^{(1)}A}_{N(Z)}=\boldsymbol{L}[\hat{\boldsymbol{q}}^{(2)}]\tilde{\boldsymbol{q}}^{(1)}=\hat{\boldsymbol{q}}^{(2)}\tilde{\boldsymbol{L}}[\tilde{\boldsymbol{q}}^{(1)}]=0. \tag{A 21}$$

This leads to the amplitude equation

$$M(Z)\frac{\mathrm{d}A}{\mathrm{d}Z}+N(Z)A=0, \tag{A 22}$$

solving which we obtain the amplitude solution $A(Z)$, which should then be expressed in terms of the fast length scale z. Finally, at first order, the response if given by

$$\boldsymbol{q}'(z)\sim A(\eta z)\hat{\boldsymbol{q}}^{(1)}(z)\exp\left(\int_0^z -k_i(z)'\,\mathrm{d}z'\right)\exp\left[\mathrm{i}\left(\int_0^z k_r(z')\,\mathrm{d}z'-\omega t\right)\right]. \tag{A 23}$$

REFERENCES

Åkervik, E., Ehrenstein, U., Gallaire, F. & Henningson, D. S. 2008 Global two-dimensional stability measures of the flat plate boundary-layer flow. *Eur. J. Mech. (B/Fluids)* **27** (5), 501–513.

Alizard, F., Cherubini, S. & Robinet, J.-C. 2009 Sensitivity and optimal forcing response in separated boundary layer flows. *Phys. Fluids* **21** (6), 064108.

Ambravaneswaran, B., Wilkes, E. D. & Basaran, O. A. 2002 Drop formation from a capillary tube: comparison of one-dimensional and two-dimensional analyses and occurrence of satellite drops. *Phys. Fluids* **14** (8), 2606–2621.

Bank, R. E., Coughran, W. M., Fichtner, W., Grosse, E. H., Rose, D. J. & Smith, R. K. 1985 Transient simulation of silicon devices and circuits. *IEEE Trans. Electron Devices* **32** (10), 1992–2007.

Basaran, O. A. 2002 Small-scale free surface flows with breakup: drop formation and emerging applications. *AIChE J.* **48** (9), 1842–1848.

Basaran, O. A., Gao, H. & Bhat, P. P. 2013 Nonstandard inkjets. *Annu. Rev. Fluid Mech.* **45**, 85–113.

Bennett, W. D., Brown, J. S., Zeman, K. L., Hu, S.-C., Scheuch, G. & Sommerer, K. 2002 Targeting delivery of aerosols to different lung regions. *J. Aerosol Med.* **15** (2), 179–188.

Boujo, E. & Gallaire, F. 2015 Sensitivity and open-loop control of stochastic response in a noise amplifier flow: the backward-facing step. *J. Fluid Mech.* **762**, 361–392.

Briggs, R. J. 1964 *Electron-stream Interaction With Plasmas*. MIT Press.

Chaudhary, K. C. & Redekopp, L. G. 1980 The nonlinear capillary instability of a liquid jet. Part 1. Theory. *J. Fluid Mech.* **96** (2), 257–274.

Consoli-Lizzi, P. A. 2016 Capillary breakup of stretched liquid jets. PhD thesis, UC3M.

Consoli-Lizzi, P. A., Coenen, W. & Sevilla, A. 2014 Experiments and non-parallel theory on the natural break-up of freely falling Newtonian liquid jets. In *APS Meeting Abstracts*.

van Deventer, H., Houben, R. & Koldeweij, R. 2013 New atomization nozzle for spray drying. *Dry. Technol.* **31** (8), 891–897.

Doshi, J. & Reneker, D. H. 1995 Electrospinning process and applications of electrospun fibers. *J. Electrostat.* **35** (2-3), 151–160.

Driessen, T. & Jeurissen, R. 2011 A regularised one-dimensional drop formation and coalescence model using a total variation diminishing (TVD) scheme on a single Eulerian grid. *Intl J. Comput. Fluid Dyn.* **25** (6), 333–343.

DRIESSEN, T., SLEUTEL, P., DIJKSMAN, F., JEURISSEN, R. & LOHSE, D. 2014 Control of jet breakup by a superposition of two Rayleigh–Plateau-unstable modes. *J. Fluid Mech.* **749**, 275–296.

EGGERS, J. & DUPONT, T. F. 1994 Drop formation in a one-dimensional approximation of the Navier–Stokes equation. *J. Fluid Mech.* **262**, 205–221.

EGGERS, J. & VILLERMAUX, E. 2008 Physics of liquid jets. *Rep. Prog. Phys.* **71** (3), 036601.

FOURES, D. P. G., CAULFIELD, C. P. & SCHMID, P. J. 2013 Localization of flow structures using ∞-norm optimization. *J. Fluid Mech.* **729**, 672–701.

FRANKEL, I. & WEIHS, D. 1985 Stability of a capillary jet with linearly increasing axial velocity (with application to shaped charges). *J. Fluid Mech.* **155**, 289–307.

FRANKEL, I. & WEIHS, D. 1987 Influence of viscosity on the capillary instability of a stretching jet. *J. Fluid Mech.* **185**, 361–383.

GALLAIRE, F. & BRUN, P.-T. 2017 Fluid dynamic instabilities: theory and application to pattern forming in complex media. *Phil. Trans. R. Soc. Lond.* A **375** (2093), 20160155.

GARCÍA, F. J. & CASTELLANOS, A. 1994 One-dimensional models for slender axisymmetric viscous liquid jets. *Phys. Fluids* **6** (8), 2676–2689.

GARNAUD, X., LESSHAFFT, L., SCHMID, P. J. & HUERRE, P. 2013 The preferred mode of incompressible jets: linear frequency response analysis. *J. Numer. Math.* **716**, 189–202.

GASTER, M., KIT, E. & WYGNANSKI, I. 1985 Large-scale structures in a forced turbulent mixing layer. *J. Fluid Mech.* **150**, 23–39.

GUERRERO, J., GONZÁLEZ, H. & GARCÍA, F. J. 2016 Spatial modes in one-dimensional models for capillary jets. *Phys. Rev.* E **93** (3), 033102.

HILBING, J. H. & HEISTER, S. D. 1996 Droplet size control in liquid jet breakup. *Phys. Fluids* **8** (6), 1574–1581.

VAN HOEVE, W., GEKLE, S., SNOEIJER, J. H., VERSLUIS, M., BRENNER, M. P. & LOHSE, D. 2010 Breakup of diminutive Rayleigh jets. *Phys. Fluids* **22** (12), 122003.

HUERRE, P. & ROSSI, M. 1998 *Hydrodynamic Instabilities in Open Flows*. Cambridge University Press.

JAVADI, A., EGGERS, J., BONN, D., HABIBI, M. & RIBE, N. M. 2013 Delayed capillary breakup of falling viscous jets. *Phys. Rev. Lett.* **110**, 144501.

KOWALEWSKI, T. A. 1996 On the separation of droplets from a liquid jet. *Fluid Dyn. Res.* **17** (3), 121–145.

LE DIZÈS, S. 1997 Global modes in falling capillary jets. *Eur. J. Mech. (*B*/Fluids)* **16**, 761–778.

LE DIZÈS, S. & VILLERMAUX, E. 2017 Capillary jet breakup by noise amplification. *J. Fluid Mech.* **810**, 281–306.

LEIB, S. J. & GOLDSTEIN, M. E. 1986 The generation of capillary instabilities on a liquid jet. *J. Fluid Mech.* **168**, 479–500.

LOSCERTALES, I. G., BARRERO, A., GUERRERO, I., CORTIJO, R., MARQUEZ, M. & GANAN-CALVO, A. M. 2002 Micro/nano encapsulation via electrified coaxial liquid jets. *Science* **295** (5560), 1695–1698.

MANTIČ-LUGO, V. & GALLAIRE, F. 2016 Saturation of the response to stochastic forcing in two-dimensional backward-facing step flow: a self-consistent approximation. *Phys. Rev.* F **1** (8), 083602.

MARÍN, A. G., CAMPO-CORTÉS, F. & GORDILLO, J. M. 2009 Generation of micron-sized drops and bubbles through viscous coflows. *Colloid. Surf.* A **344** (1–3), 2–7.

MARQUET, O. & SIPP, D. 2010 Global sustained perturbations in a backward-facing step flow. *Seventh IUTAM Symp. Laminar-Turbulent Transition* **18**, 525–528.

MONOKROUSOS, A., ÅKERVIK, E., BRANDT, L. & HENNINGSON, D. S. 2010 Global three-dimensional optimal disturbances in the Blasius boundary-layer flow using time-steppers. *J. Fluid Mech.* **650**, 181–214.

NICHOLS, J. & LELE, S. 2010 Global mode analysis of turbulent high-speed jets. In *Annual Research Briefs 2010, Center for Turbulence Research.*

NICHOLS, J. W. & LELE, S. K. 2011 Non-normal global modes of high-speed jets. *Intl J. Spray. Combust. Dyn.* **3** (4), 285–301.

PEARSON, J. R. A. & MATOVICH, M. A. 1969 Spinning a molten threadline. Stability. *Ind. Engng Chem. Res.* **8** (4), 605–609.

PLATEAU, J. A. F. 1873 *Statique expérimentale et théorique des liquides soumis aux seules forces moléculaires*, vol. 2. Gauthier-Villars.

RAYLEIGH, LORD 1879 On the capillary phenomena of jets. *Proc. R. Soc. Lond.* A **29** (196–199), 71–97.

RUBIO-RUBIO, M., SEVILLA, A. & GORDILLO, J. M. 2013 On the thinnest steady threads obtained by gravitational stretching of capillary jets. *J. Fluid Mech.* **729**, 471–483.

SAUTER, U. S. & BUGGISCH, H. W. 2005 Stability of initially slow viscous jets driven by gravity. *J. Fluid Mech.* **533**, 237–257.

SCHMID, P. J. 2007 Nonmodal stability theory. *Annu. Rev. Fluid Mech.* **39** (1), 129–162.

SCHMID, P. J. & HENNINGSON, D. S. 1994 Optimal energy density growth in Hagen–Poiseuille flow. *J. Fluid Mech.* **277**, 197–225.

SENCHENKO, S. & BOHR, T. 2005 Shape and stability of a viscous thread. *Phys. Rev.* E **71** (5), 056301.

SEVILLA, A. 2011 The effect of viscous relaxation on the spatiotemporal stability of capillary jets. *J. Fluid Mech.* **684**, 204–226.

SHIMOZURU, D. 1994 Physical parameters governing the formation of Pele's hair and tears. *Bull. Volcanol.* **56** (3), 217–219.

SIPP, D. & MARQUET, O. 2013 Characterization of noise amplifiers with global singular modes: the case of the leading-edge flat-plate boundary layer. *Theor. Comput. Fluid Dyn.* **27** (5), 617–635.

SPALDING, D. B. 1972 A novel finite difference formulation for differential expressions involving both first and second derivatives. *Intl J. Numer. Meth. Engng* **4** (4), 551–559.

TOMOTIKA, S. 1936 Breaking up of a drop of viscous liquid immersed in another viscous fluid which is extending at a uniform rate. *Proc. R. Soc. Lond.* A **153** (879), 302–318.

TREFETHEN, L. N., TREFETHEN, A. E., REDDY, S. C. & DRISCOLL, T. A. 1993 Hydrodynamic stability without eigenvalues. *Science* **261** (5121), 578–584.

VIOLA, F., ARRATIA, C. & GALLAIRE, F. 2016 Mode selection in trailing vortices: harmonic response of the non-parallel batchelor vortex. *J. Fluid Mech.* **790**, 523–552.

WIJSHOFF, H. 2010 The dynamics of the piezo inkjet printhead operation. *Phys. Rep.* **491** (4–5), 77–177.